Stabilization of Unstable Equilibria in Bistable Structures

Tyler van Iderstein

A thesis
submitted in partial fulfillment of:
requirements for the degree of

Master of Science in Civil Engineering

University of Washington

2018

Committee:
Richard Wiebe
Michael Motley
Tyler Sprague

Program Authorized to Offer Degree:
Civil and Environmental Engineering

University of Washington

Abstract

Stabilization of Unstable Equilibria in Bistable Structures

Tyler van Iderstein

Chair of the Supervisory Committee:
Assistant Professor Richard Wiebe
Civil and Environmental Engineering

Snap-through buckling provides an intricate force-displacement relationship for study. With the possibility for multiple limit points and pitchfork bifurcations and large regions of instability, experimental validation of numerical analysis can become difficult. This requires stabilization of unstable static equilibria, for which limited prior research exists. For all but the simplest cases, more than one actuator is needed, increasing the complexity of the experiment to the point of intractability without a control system.

In this thesis, the necessary conditions for stabilization of a buckled beam with pinned boundaries under transverse loading were determined. By combining various nonlinear solution methods, a control system was created that could stabilize any branch of the force-displacement response. Experimental traversal of an unstable branch are presented along with other unstable static equilibrium configurations. The control system had numerical limitations, losing convergence near singular points. The groundwork for experimental stabilization was validated and demonstrated.

Keywords: stability, nonlinear mechanics, snap-through buckling, experimental mechanics, control system

Acknowledgments

I would like to express my sincerest thanks to everyone who has helped me complete this thesis. First, thank you to my advisor and committee chair Dr. Richard Wiebe for his excellent guidance and trust. Thank you for teaching me how to ask the right questions and accept that research does not always go as planned. You have given me the skills and knowledge to go confidently into my engineering career. Never stop giving your students toy problems to investigate.

I would like to thank Dr. Michael Motley for his instruction and guidance. Your stability and finite element analysis classes provided a fantastic foundation to build my research off. Thank you for being available when I had concerns and giving pragmatic advice.

I would like to thank Dr. Tyler Sprague, P.E., for his willingness to foster collaboration between architecture and structural engineering. The project you provided was intriguing and made me think about my own research in a new way. I hope you continue to push for greater collaboration and show us engineers how to appreciate the beauty that we help bring to life.

I would like to thank my office-mates Pavel, Tom, and Jakob. You guys were there every day and made my experience here at UW great. We may have had too much fun together, but we still got done what we needed to. More 313B may have been a weird room, but it was our room.

I would like to recognize all of my other fellow classmates and peers for being a huge part of my life in Seattle. You all got me through my classes, research, lunch breaks, and boredom. Andrew and Han-Gyu, you both rounded out a great research group. Best of luck on your continued studies.

Lastly, I must thank my family. I would not be here without your lifelong support and encouragement. I dedicate this work to my large and crazy family who always pushed me to be something greater than I was. I know I have made you proud (because you keep telling me) and I will continue to do so. I told you I wanted to be a rocket engineer when I was little. Well, here I am, and I'd say I got close enough.

Contents

List of Figures

List of Tables

Chapter 1

Introduction

1.1 Motivation

Unstable systems are inherently difficult to conduct experiments on, since the behavior of interest is usually transient and easily disturbed. This research was inspired by the work presented in [1–3], in which the development and implementation of non-invasive dynamic control systems were discussed. These used the arc length method to stabilize unstable periodic responses of a vibrating structure. The arc length method is a powerful nonlinear solution method developed by Riks [4] and Crisfield [5]. Thus, the question driving this work was, if unstable dynamic responses could be stabilized by a control system, could a similar result be achieved for unstable static tests? In addition, is the arc length method the correct method to base this controls system on?

Snap-through buckling is an excellent phenomenon to analyze to answer these questions. This response is characterized by two remote stable configurations separated by a region of instability. Numerous limit and bifurcation points can exist within this unstable region. When bifurcated branches appear, the structure now has multiple paths it can follow, each at a different energy level. These higher energy unstable equilibria are saddle points in the energy surface and guide the dynamic response of the system. This provides a perfect opportunity to develop stabilization techniques and experimental control systems.

Experimental work on static snap-through response has relied on relatively simple methods thus far. These have included load control [6], displacement control of one point [7–9], and constraining the beam between two rigid plates separated by a gap [10]. Using dynamic loading and digital image correlation, a single unstable equilibrium configuration was found in [11]. The proposed research expands the scope for quasi-static snap-through buckling tests and enables further exploration into the interaction between static and dynamic response.

1.2 Outline

This research covers the theory, application, and experimental verification of a method for stabilizing unstable static equilibria. The primary objectives are: (1) identify conditions that lead to unstable static configurations becoming stable, (2) apply these conditions to a class of structures exhibiting snap-through buckling, (3) design an experiment utilizing a control system designed to follow unstable force-displacement curves, and (4) conduct experiments to verify these predictions. A secondary objective is to develop a series of demonstrations for undergraduate structural analysis classes using the testing equipment and control system developed for the primary research.

The research presented is significant for its contributions to experimental methods related to unstable structures and snap-through buckling. The concepts discussed in this research can be applied to experiments on other classes of unstable structures. Within the field of snap-through buckling, the ability to stabilize unstable equilibria opens new opportunities to study the relationship between static and dynamic response.

This thesis is organized as follows: Chapter 2 presents the theoretical foundation for the stabilization of unstable equilibria. The general stability concepts that lead to this stabilization are discussed. Stability of an initially flat buckled beam under transverse load is detailed. The stabilization concepts are applied to this structure as a case study. Practical limitations and implementation are discussed. Chapter 3 covers the development of an experimental setup to stabilize unstable equilibria in a buckled beam exhibiting snap-through buckling. The hardware used in the experiment is detailed. Various experimental control systems and their shortcomings are detailed. The final control system is presented. Chapter 4 presents the experimental results using the experimental control system. Results verifying the stabilization theory are presented. The results of the class demonstrations are also discussed. Chapter 5 summarizes the research and provides recommendations for further research.

Chapter 2

Effects of Constraints on Stability

This chapter details the theory and methodology for stabilizing unstable branches of a force-displacement curve using additional displacement constraints. The methodology is applied to a buckled beam exhibiting snap-through buckling.

2.1 Elimination of Unstable Modes

In accordance with the principle of minimum potential energy, a stable equilibrium configuration will have only positive eigenvalues. Similarly, an unstable equilibrium configuration has at least one negative eigenvalue and an associated unstable mode shape. This mode shape can be thought of as an escape route for the system; the infinitesimal displacement the system goes through to assume a lower energy state will be in the form of the unstable mode with the lowest eigenvalue. Note, this is not the displaced shape of the resulting stable equilibrium configuration, only the initial displacement from the unstable configuration.

To stabilize an unstable configuration, the clearest course of action is to prevent unstable modes from manifesting. When all possible escape routes are eliminated, the system must be stable. Since each mode shape affects every degree of freedom in the structure, it is impossible to remove an arbitrary mode without affecting the rest of the modes in the system. An unstable structure will exhibit some transient response, either moving to a lower energy state or failing. By preventing this dynamic response in a way that does not change the internal state of the structure, the configuration has been stabilized.

An analogy for this idea is balancing a ball on a hilltop or saddle point. In either location, the ball is at an unstable equilibrium, rolling downhill with the slightest perturbation. For the case of the saddle, if a displacement constraint were added in the downhill direction, the ball would be stable, settling into the low point of the remaining valley. The state of the system is indistinguishable from the unconstrained version, but stability is now ensured. Similarly, preventing motion in the x and y directions for a ball balanced on a hilltop does not induce reaction forces and the system is no longer at risk of rolling downhill.

Unstable modes of continuous systems are difficult to isolate, but their effects can be mitigated with simple constraints. Since a mode shape is the form of the displacement of the structure from its current configuration, adding displacement constraints at strategic points can remove a mode as an escape route. Any other mode that needs displacements in the constrained directions will also be eliminated. New mode shapes conforming to the new set of boundary conditions will replace the mitigated ones and hopefully be stable. If all unstable modes can be mitigated, the unstable equilibrium configuration becomes stable.

If one wishes to stabilize an unstable static equilibrium path, every point along it must be stabilized. This requires the displacement constraints to be moved with the structure to ensure the no reaction condition. Since finding a new set of constraint positions for each equilibrium point is impractical, it may be necessary to determine a set of constraint positions that will be used for all points. The evolution of unstable modes along the path will have to be taken into account.

2.2 Snap-Through Buckling

As an illustration of how the stability of a system can be manipulated, consider a structure exhibiting snap-through buckling. An initially flat, buckled beam with pin-pin boundary conditions, a point load at midspan, shown in Fig. 2.1, and properties given in Table 2.1 will be used for the remainder of this chapter to motivate the discussion. The theoretical results are based on a formulation detailed in Appendix A. This formulation represents a large portion of the theoretical work done in this thesis. The formulation was used to develop a new finite element code in MATLAB as opposed to commercially available software. This allowed better access to internal variables (e.g. tangent stiffness) and provided necessary background for later experiments on snap-through buckling.

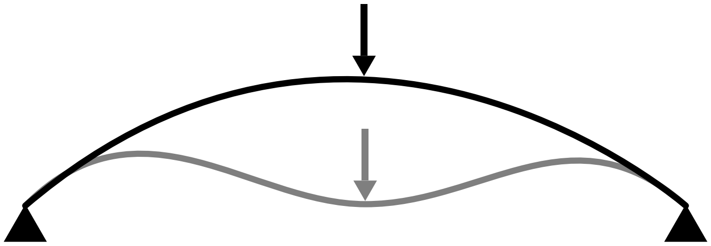

Figure 2.1: Buckled beam with point load that exhibits snap-through buckling

Table 2.1: Example Beam Properties

Length (mm)	304.8
Moment of Intertia (mm^4)	0.1387438
Area (mm^2)	0.32258
Modulus of Elasticity (GPa)	206.843
Density (kg/m^3)	1500
Initial Rise (mm)	6

The force-displacement relationship for this beam in Fig. 2.2 shows the distinctive features of snap-through buckling. Eight critical points exist for this structure, four limit points and four bifurcation points. The limit points are the defining attribute for snap-through buckling, where the system loses stability and violently snaps to a remote configuration that is able to carry the load. This particular configuration also exhibits multiple bifurcations, where the displaced shape of the structure depends on which path is followed. The branches can be placed into two categories based on displaced shape: symmetric and asymmetric. The continuous looping path consists of only symmetric displaced shapes, while the bifurcated paths are asymmetric. The asymmetric paths come in mirror-image pairs for this class of structure. The order in which the limit and bifurcated paths come is dependent on the initial rise and stiffness of the system.

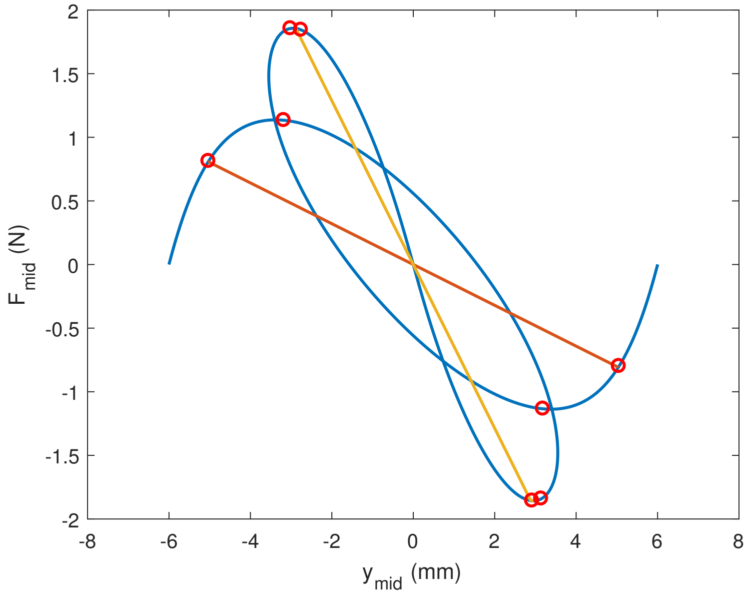

Figure 2.2: Force-displacement curve with two limit points and two bifurcated paths showing all critical points

Each asymmetric branch emanates from a symmetric branch and is at a lower energy. In Fig. 2.3, these asymmetric bifurcated branches appear as shortcuts across the energy space. When they exist, the lower energy asymmetric shapes will be the preferred shape for the structure. This means that any symmetric displaced shape will be inherently unstable, along with all higher energy branches that exist.

At each equilibrium point, the stability of the system can be checked. Since a system

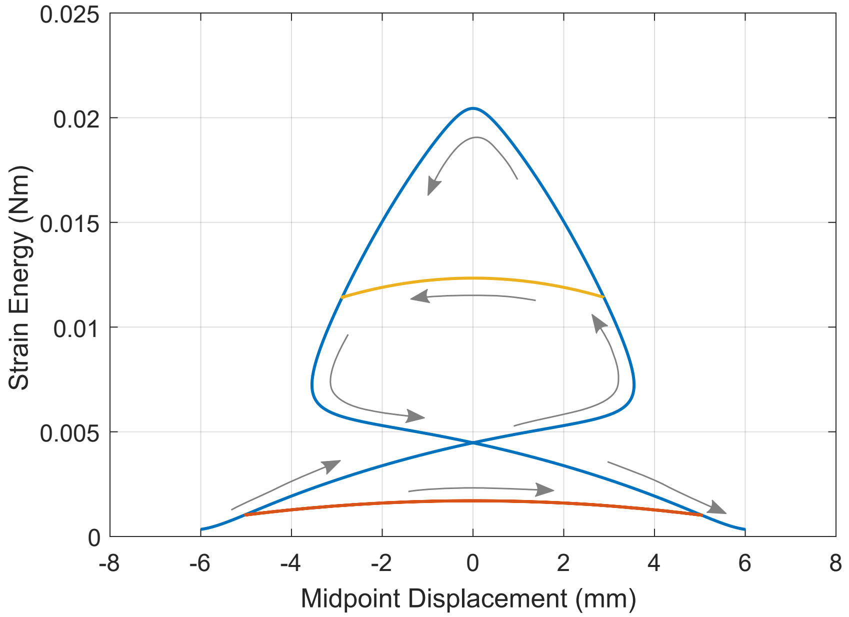

Figure 2.3: Internal strain energy vs. midpoint displacement showing bifurcated branch shortcuts, arrows correspond to force-displacement curve traversal

is only stable if all of the eigenvalues of the stiffness are positive, calculating the lowest eigenvalue is the only check needed. Calculating more modes gives an interesting relationship. Each time the force-displacement curve passes through a critical point, an eigenvalue becomes negative and a new unstable mode appears. The first critical point in Fig. 2.2 occurs at ±5 mm, so the system is unstable for midpoint displacements between −5 mm and +5 mm and stable everywhere else. The first bifurcated branch does not encounter another critical point, so there is only one unstable mode along that path. Along the symmetric branch, a second unstable mode appears at ±3.5 mm and a third at ±3 mm. The fourth unstable mode appears on the symmetric branch after the bifurcation point at ±3 mm. See Fig. 2.4 for a plot of the mode shapes at selected points along the curve.

This class of structure has interesting relations to classical Euler buckling. In [12], the authors observed for this same class of structure that, for low rises, the displaced shapes at the zero transverse load crossings are approximately pure Euler buckling mode shapes. In addition, the zero transverse load crossings appear to occur at the same displacement for any one-parameter loading. In the absence of transverse loading, the situation is indistinguishable from an Euler buckling problem, so the lowest energy configuration would be the nearest Euler buckling mode. The zero transverse load crossings (ZTLC) for the example response and their first four mode shapes are shown in Fig. 2.4. The mode shapes appear to approximate Euler buckling modes. A pattern emerges in which modes have negative eigenvalues, which will be employed in the next section.

The mode shapes and eigenvalues were found by calculating the natural frequencies in the deformed configuration. To satisfy the principle of minimum potential energy, the potential energy surface must have a positive second derivative to be stable. An equivalent way to frame this problem is to look at the response of the system to small oscillations by solving the eigenproblem $(\mathbf{K} - \omega_n^2\mathbf{M})\,\phi_n = \mathbf{0}$. If ω_n^2 is negative, the motion of the system becomes unbounded due to ϕ_n. Since the mass matrix is always positive definite, ω^2 will change sign as K becomes indefinite, agreeing with the principle of minimum potential energy.

2.3 Application of Stabilization Concepts

Having identified key behaviors of a buckled beam under transverse loading, the stabilization concepts discussed in Sect. 2.1 can be applied to this class of structures. This will be discussed in two parts: stabilization of points near the zero transverse load crossing and extending the results to entire branches of the force-displacement curve.

In structural design, a common way to strengthen an axially loaded member against buckling is to add a support somewhere in the span, by framing another member in or tying it to other parts of the structure. This reduces the unbraced length of the member, raising the Euler buckling load. Placing a displacement constraint at midspan cuts the unsupported

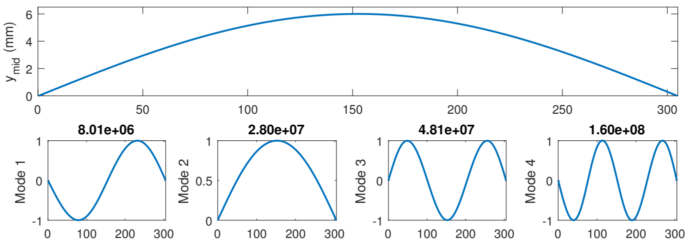

(a) ZTLC 1

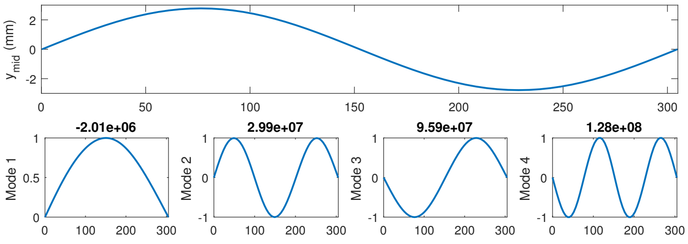

(b) ZTLC 2

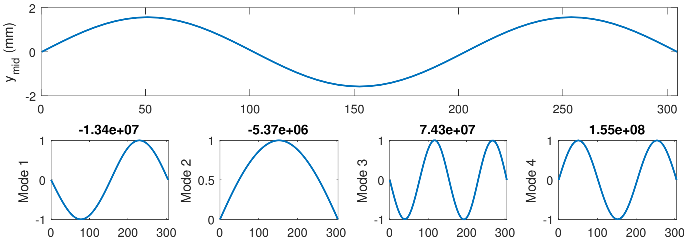

(c) ZTLC 3

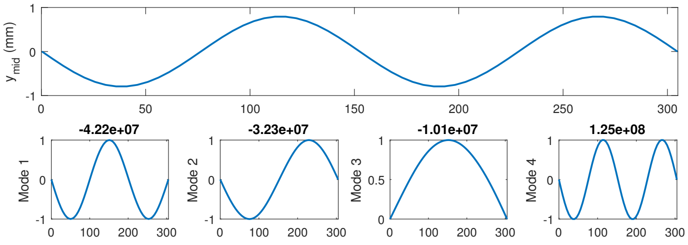

(d) ZTLC 4

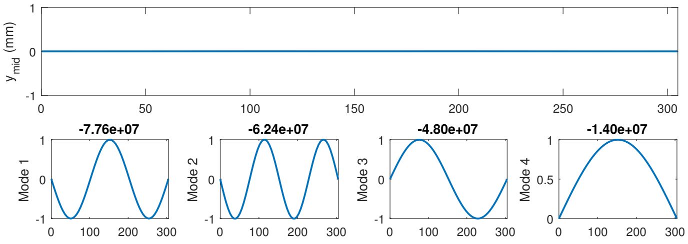

(e) ZTLC 5

Figure 2.4: Displaced shape and first four mode shapes at each ZTLC

length in half, quadrupling the buckling load. This value happens to be the second Euler buckling load of the original unsupported member. This relationship is true for all equal divisions of a member with pin-pin boundary conditions in buckling.

$$P_{e,n} = \frac{n^2\pi^2 EI}{L^2} = \frac{\pi^2 EI}{(L/n)^2} \quad \text{n=1,2,3,...} \tag{2.1}$$

Likewise, the combined shape of the equally divided members is the same as the corresponding higher mode shape for the original member.

$$\phi_n(x) = \sin\left(\frac{n\pi x}{L}\right) = \sin\left(\frac{\pi x}{L/n}\right) \quad \text{n=1,2,3,...} \tag{2.2}$$

Both of these relations assume the constraint does not inhibit rotation.

If one wishes to stabilize a zero transverse load crossings for the class of buckled beams under consideration, the problem reduces to stabilizing the proper Euler buckling mode. By stabilizing the zero transverse load crossing of the desired branch, all lower energy zero crossings will also become stable. This guarantees that one point along every branch can be stabilized.

Stabilization of an entire curve comes through observations of the unstable modes of the structure. There are no closed-form equations for the response of these buckled beams under transverse loading, so analysis is limited to nonlinear finite element analysis or reduced order models. As noted earlier, unstable modes are only introduced at limit or bifurcation points, so along any given branch, the set of unstable modes is fixed. The structure does not resemble any Euler buckling mode shape at points far away from the zero transverse load crossing, but the unstable mode shapes of the structure appear to approximate Euler mode shapes when no extra constraints are applied. As more constraints are added, the modes lose their resemblance to the Euler mode shapes, as seen in Fig. 2.5 for the point (-1.76mm, 1.14N) on the second bifurcated branch. Furthermore, the unstable mode shapes of the unconstrained system all appear to be approximately the set of Euler mode shapes of lower order than the displaced shape at the zero transverse load crossing of the given branch.

Since the equal-division constraint locations exclude all lower Euler buckling modes as escape routes for the zero transverse load crossings, it stands to reason that using the same constraints elsewhere along the branch will prevent mode shapes that approximate the Euler modes as well. A beneficial side effect is all lower energy branches could be stabilized if this is true, since the branches share the same set of possible unstable modes. The author is not aware of a way to prove this fact in general, but this observation holds true for the structure considered in Fig. 2.1.

The four force-displacement curves in Fig. 2.6 show the stability of the structure at each point along the curve under different equal-subdivision constraint combinations. Each set of constraints stabilizes the Euler buckling mode that best approximates the ZTLC on one of the branches, as suggested by Eqs. 2.1 and 2.2. The constraint set [L/3, 2L/3] in Fig. 2.6 does not stabilize the entire second symmetric branch because there were not nodes available at the exact third points in the model. The other plots indicate proper node locations would stabilize the entire branch.

Though the equal division points appear to be the optimal constraint positions, they are not unique. A mode can be prevented by placing constraints in numerous locations. At the point (2.88mm, -0.68N), along the first symmetric branch, the lowest eigenvalue was calculated with a constraint at the midpoint and two constraints at every combination of the 61 nodes in the mesh. A plot of the positive eigenvalues is shown in Figure 2.7, giving only the combinations that result in a stabilized state. The optimal constraints for this branch according to the Euler buckling approximation are at [L/3, 2L/3]. Since one constraint was kept at the midpoint, this combination does not exist. According to the plot, the highest eigenvalue can be achieved with constraints at [L/4, L/2, 3L/4], which corresponds to the next highest equal subdivision. However, other combinations are stable.

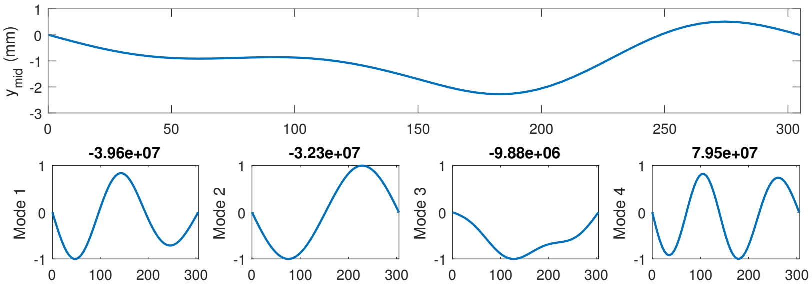

(a) No additional constraints

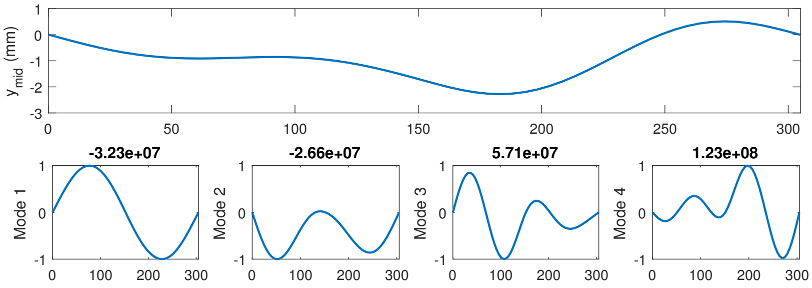

(b) Constraint at L/2

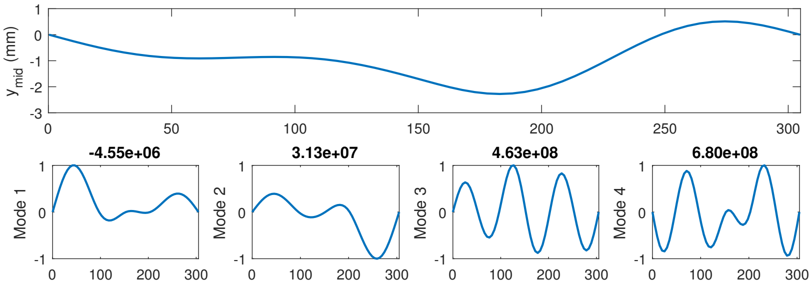

(c) Constraints near L/3 and 2L/3

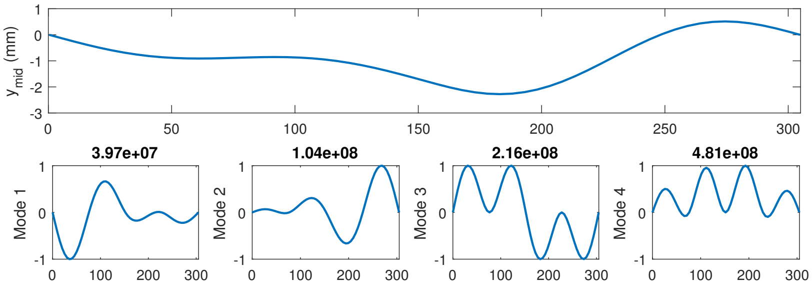

(d) Constraints at L/4, L/2, and 3L/4

Figure 2.5: Displaced shape and first four mode shapes and eigenvalues at (-1.76mm, 1.14N) under different equal-subdivision constraints

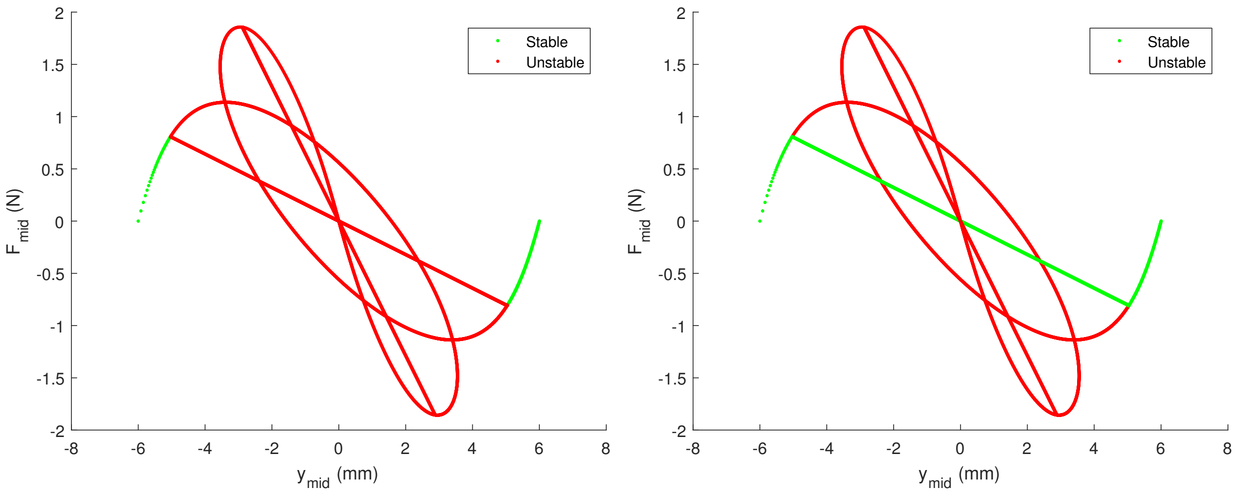

(a) No additional constraints (b) Constraint at L/2

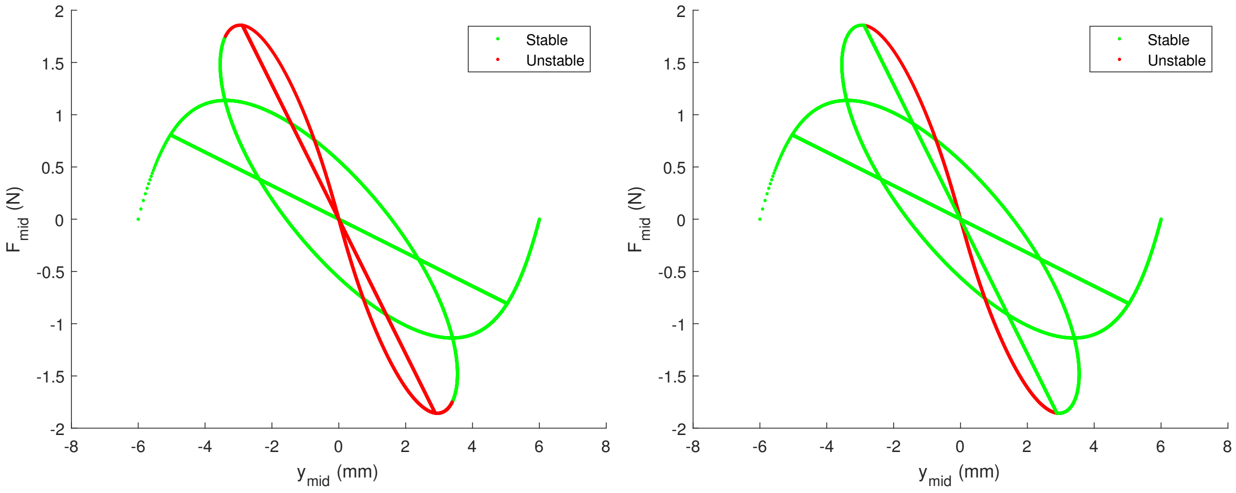

(c) Constraints near L/3 and 2L/3 (d) Constraints at L/4, L/2, and 3L/4

Figure 2.6: Stability of structure under different equal-subdivision constraints

Placing the side constraints away from the center or ends results in stabilization in this configuration. If the two movable constraints are at the same node, they act as one constraint. For one constraint between L/6 and L/3 and the other at L/2, the system can be stabilized. Increasing the magnitude of the load slightly to the point (3.2mm, -0.93N), no combination of two constraints exist that stabilize the structure.

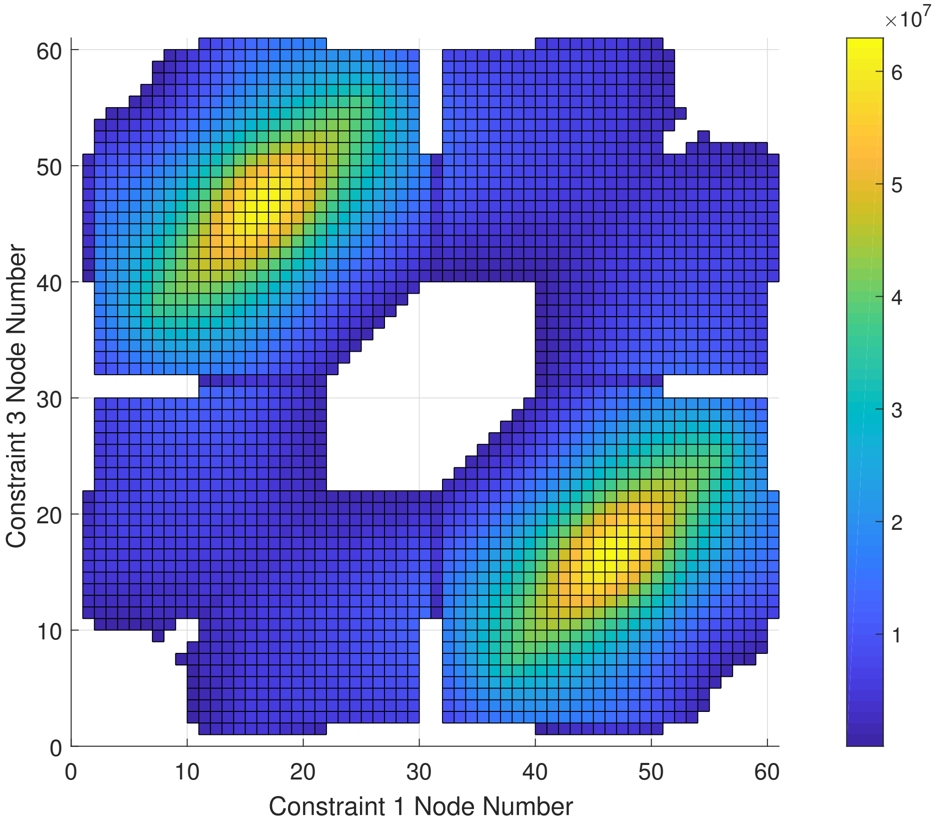

Figure 2.7: Value of lowest eigenvalue at one point for two constraints placed at all FEM node combinations and one constraint at L/2 for the point (2.88mm, -0.68N)

Chapter 3

Experimental Design and Fabrication

3.1 Experimental Applications of Stabilization

The ability to stabilize unstable systems provides a framework to design experiments that replicate the necessary conditions. From a theoretical perspective, a movable displacement constraint is contrived, but a linear actuator satisfies this condition exactly. By attaching the actuators at the predicted points, the corresponding unstable modes will be stabilized.

Experimental work on snap-through buckling has relied on stabilization for many years. Many experiments used one actuator to apply load to the beam, which provided a constraint that stabilized the lowest energy unstable mode. An excellent example of this can be seen in [9]. The difficulty of running an experiment increases drastically when more than one actuator is present. The additional constraints must have no reaction in an equilibrium configuration to ensure non-invasive control. To achieve this, significant manual input or a sophisticated control system to achieve.

To validate the stabilization predictions in 3 regarding a buckled beam with a central point load, an experiment was designed with the goal of stabilizing the first unstable symmetric branch. The use of a control system was necessary since at least two actuators were needed to stabilize the branch. This provided an opportunity to test whether the arc length method is a viable control method for quasi-static testing.

3.2 Design of Test Frame

The final test frame is shown in Fig. 3.1. Three actuators were needed to stabilize the desired unstable branch. One actuator was required at the center to apply the load and measure the midpoint displacement, and the side actuators provided displacement constraint only. At each equilibrium point, the reaction at these two actuators would be zero. In addition, the relative displacements of the actuators would inform which branch of the response the structure was on.

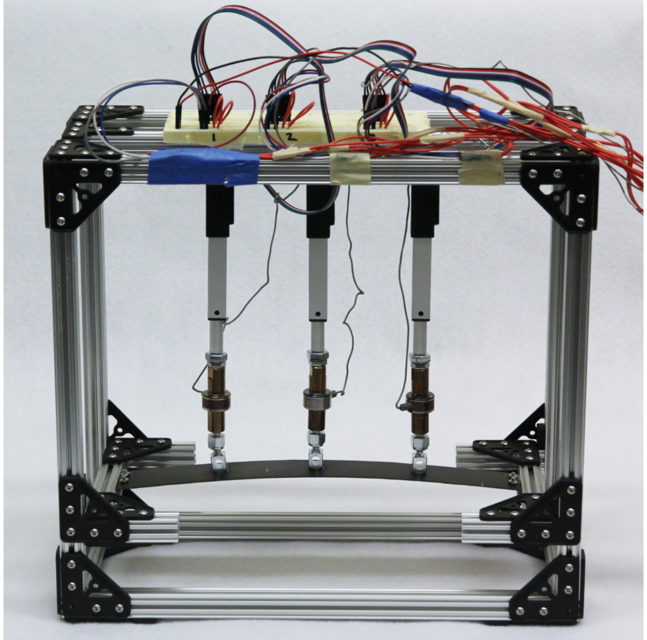

Figure 3.1: Experimental setup with specimen attached

3.2.1 OpenBeam

The loading frame used in the experiments was built from a modular extruded aluminum kit sold by OpenBeam. The kit came with members in a variety of pre-cut lengths and all the connections and bolts needed for assembly. No cutting was required, but the provided lengths put a constraint on the size of the frame. The final dimensions of the frame were

13x6x12 inches. A specimen 10.5 inches in length could fit between the supports and have a maximum height of 9 inches.

A modular beam kit was used to allow a variety of specimens and tests to be conducted. The end supports could be moved vertically to allow specimens and equipment of different heights, and the supports could be moved to allow variable span distances. If boundary conditions or equipment required it, individual parts of the frame could be removed and replaced. As frames for low-load tests (in the range of 10-20 pounds) are not commonly built and the setup time for this frame was relatively fast, it was also utilized by other researchers for quick experimental tests and verification. Examples of these can be found in Appendix (whichever appendix has this stuff).

Three boundary condition methods were used to test beam specimens in this frame. To obtain a fixed end, the specimen was clamped to the frame support. This was sufficient for small deformations, but slipping could occur if large axial loads or large displacements were applied. If the clamp was removed, the specimen could rotate about the corner of the support, allowing for a pinned end condition. Large vertical displacements were possible since the specimen could slide on the supports. However, the beam could only be pushed, as it would come off the supports. Complete testing of response with snap-through requires being able to pull on the beam as well. Small piano hinges were bolted to the specimen and the frame to allow rotation while still carrying shear in both directions. A close-up picture of the hinges is sown in Fig. 3.2.

3.2.2 Carbon Fiber Beam

The beam specimen used was made of a carbon fiber-epoxy composite. This material was chosen over steel or aluminum for two main reasons. First, carbon fiber does not yield, so repeated testing would not cause unseen damage to the specimen. Second, the bending stiffness can be changed by using a different layup without changing the thickness or width.

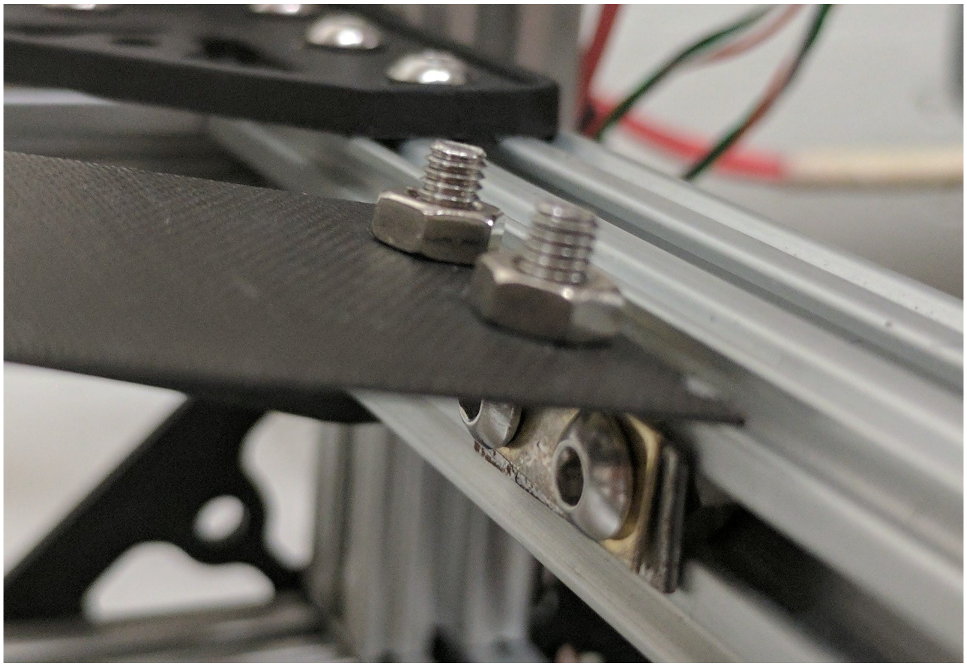

Figure 3.2: Detail of pin boundary condition using piano hinge

The stiffness of the beam was dictated by the capacities of the other components in the test fixture. The frame could accommodate a specimen of about 300mm between supports, and the maximum buckled rise was limited by the actuator stroke to about 40mm. The limit point buckling load for this geometry had to be below the load capacities of the actuator. After doing a design study on the flexural stiffness (EI) needed, a number of layups were cured and tested to account for manufacturing variance. The one with the closest stiffness to the desired stiffness was selected. The final beam properties can be found in Table 3.1.

Table 3.1: Experimental Beam Specimen Properties

Layup	$[0\,90\,0]_S$
Length (mm)	304.8
Width (mm)	30
Thickness (mm)	0.58
E_{xx} (GPa)	108

3.2.3 Actuators

Three Actuonix L12-I linear actuators were used in this test frame. This model was selected because it has an integrated controller, potentiometer feedback, and was the most cost-effective product for the needed size. The product can be configured with a variety of stroke lengths, gearing ratios, and operating voltages. The configuration selected is detailed in Table 3.2. These were attached to the testing frame with the included brackets.

Table 3.2: Actuonix L12-I Details

Stroke (mm)	50
Gear Ratio	210:1
Control Voltage (V)	6
Backdrive Force (N)	45
Mechanical Backlash (mm)	0.2
Repeatability (mm)	0.3

Using these actuators in LabVIEW was relatively simple. Both the control and feedback systems used a proportional voltage method. A voltage in the 0-5V range is applied proportional to the desired stroke. The feedback is given proportionally in the 0-3.3V range. In testing, the controller did not extend the actuator to the proper length when set to under 25mm. The feedback would return the actual stroke through the full range, so a simple feedback loop was added to correct the controller error.

The target market for these actuators is low-cost robotics and automation, so high-resolution accuracy could not be expected. However, the resolution was sufficient for the goals of this research. The position could be set and read with a margin of error of 1mm with feedback correction active. Friction in the internal screw drive would limit small movements at loads higher than 12N, setting the highest possible limit load. Deflection due to backlash was visible under load reversal, even if the actuator itself was not moving. For larger displacements, the feedback could be read as the stroke increased, resulting in smoother data than moving incrementally.

3.2.4 Load Cells

The load cells used were Honeywell Model 34, two with a 5lb (22N) capacity and one with a 10lb (45N) capacity. The 10lb actuator was attached to the middle actuator, and the two 5lb actuators were attached to the side actuators. Higher loads were expected in the middle than on the sides, resulting in this layout.

These load cells had female threads on each end, making them easy to attach to the other components. The ends of the actuators were also threaded, so two bolts were superglued together to create a connecting rod between the different threads. Any threaded connection could be attached to the other end to interface with the specimen.

Amplifiers were used to increase the resolution of the data. After calibration, the load cells could resolve a change in load of 0.1 N. However, they were very sensitive to noise in the electrical line. Depending on the power outlet, the load cell data could be so noisy the results were unusable. Fortunately, the majority of the testing was carried out where there was less noise.

3.2.5 Pin Connection

Connecting the beam to the load cell was a challenge. The tests required an ideal pin connection that could carry both tension and compression but only attached from one side. Early attempts did not work: bolting the beam to the actuator prevented rotation and pushing on the beam with the load cell only carried compression. Supporting the beam from both above and below was not possible with the actuators.

Two working connections were made. The first was a slot cut the size of the specimen cut into another piece of material and attached to the load cell with a bolt. It worked well for small displacements and no load reversal, but it didn't work for large displacements. The beam could slide and rotate within the slot and move vertically under load reversal because

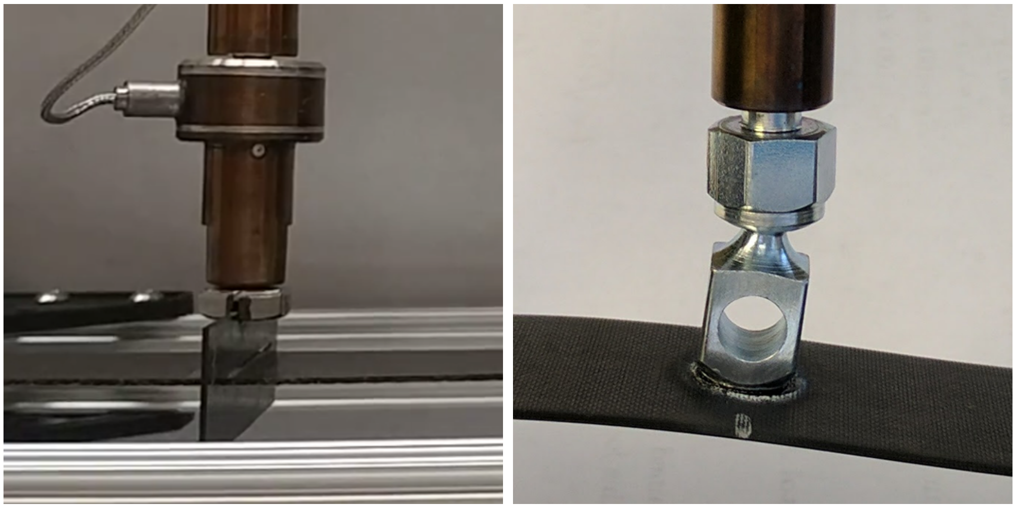

(a) Slot connection, not used (b) Rod-end connection, used in testing

Figure 3.3: Two versions of pin connections for testing

the slot was not cut exactly. The material was also thick enough to prevent large rotations of the beam. A new slot would have to be cut for each specimen, so this design was scrapped.

The second connection was a swivel-shaft rod end purchased from McMaster-Carr, product 6058K13. These were ball joints with a threaded shaft at one end and a flat surface at the other. The threaded end screwed into the load cell and the flat end was glued to the surface of the beam, creating a secure connection. For the given geometry, the beam did not rotate far enough to encounter the rotation limits of the ball-and-socket joint. Friction was the most significant problem with this joint. Even after lubrication, the joints could stick enough to prevent small rotations. This caused hysteretic effects in the rotation at the joint when returning to the same displaced configuration. However, this effect did not affect the results significantly. The two connections are shown in Fig. 3.3.

3.3 Experimental Validation

With a working test frame, experimental validation of the numerical model could be conducted. The specimen was buckled and a transverse load was applied at midspan. As two stable equilibria exist, the experiment was conducted twice, starting from each of the equilibria and moving to the other.

Using the material properties of the specimen, the experiment was modeled using the same load case with the load applied one node off-center to approximate the bifurcation paths. As seen in Fig. 3.4, the model accurately predicts the bifurcation point buckling load and location. As expected, the first bifurcation path was followed instead of the primary path. Deviations from the prediction were likely caused by geometric imperfections in the experiment or variations in material properties.

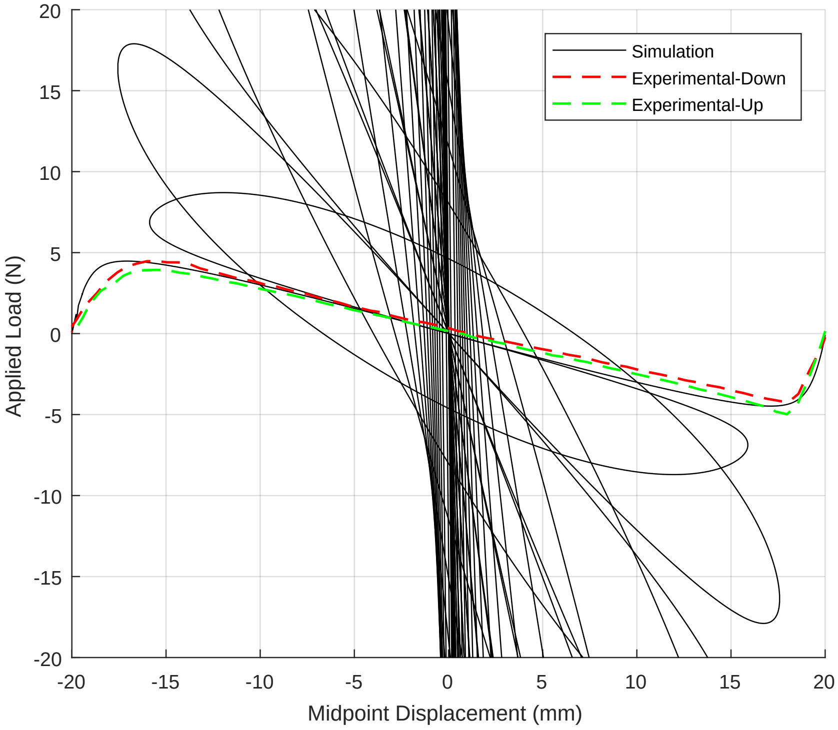

Figure 3.4: Experimental validation of numerical model

3.4 Control System Formulations

Many numerical methods are available to adapt for an experimental control system. Many of the limitations from a numerical perspective are also present in an experimental setting. Each method in this section was implemented in some form during the course of this research. Determining if the arc length method was a viable method was of special interest. This section gives a summary of each common method along with experimental accommodations.

3.4.1 Manual Control

Though not a real control system, manual control is the best place to start with unfamiliar phenomena. Prototyping a simulation or experiment leads to a better understanding of the behavior of the system. Whether inputting random numbers, educated guesses, or estimations, manually perturbing a numerical model is the best way to find its limitations. Similarly, many observations can be made with a prototype model before committing to a more expensive, high accuracy test. Obviously, the amount of work possible with manual control and prototypes is limited, but the payoff once more sophisticated methods are introduced is significant.

In the course of this research, two manual processes significantly improved the automated work. First, having a narrow piece of carbon fiber on hand was indispensable for understanding the behavior of buckled beams undergoing snap-through. Having a physical model to compare numerical results against and to demo during meetings moved the project forward quickly. Second, spending time understanding how the actuators worked informed the final control system. Manually setting the actuator positions provided bounds on the hardware and experimental space. Avoiding damage to the setup is easier with direct control.

3.4.2 Displacement Control

Displacement control is given by a constraint like $\Delta_j = \Delta_j(t)$, where the displacement history of one point is specified. The loading and internal stress state that would result in that displacement can be determined. Care must be taken in assuming a displacement history, since the real structure may deviate from it. If a nonsensical choice is made, the method will return equilibrium configurations that have no bearing on the real response of the structure. When a displacement tangency occurs, the solution will fail. At a bifurcation point, the system will want to take the lowest energy state, so unstable regions cannot be explored. Modeling a test is generally done with the same control method used in the test. Actuators are generally displacement controlled, so tests that utilize them must be inherently displacement controlled, along with the models of the results. Experiments are limited by the displacement capacity of the hardware and the accuracy of the assumed displacement history.

3.4.3 Load Control

Load control is parameterized as $\mathbf{F_{ext}} = \lambda(t)\mathbf{F}$, a constant load pattern magnified by a scaling history. The Newton-Raphson method is one of the most widely used nonlinear numerical solution algorithms and is based on a monotonic change in load. Most loading scenarios are imposed loads, giving a wider variety of simulation cases than displacement control. The algorithm breaks down where the system stiffness changes rapidly or becomes singular, such as buckling, cracking, and collapse. The method also has convergence problems for hardening responses. In an experimental setup, load control is more primitive. Using weights, pressure, electromagnets, or hydraulic rams, variable loads can be applied to a specimen, but sudden loss of stiffness can cause significant damage. In snap-through buckling under load control, the system snaps dynamically to a remote configuration, which is difficult to control.

3.4.4 Arc Length Control

The arc length method is a newer numerical method developed specifically to address the limitations of load and displacement control when analyzing systems exhibiting load or displacement tangencies. Rather than specifying a load or displacement, the arc length constraint defines a relationship between the two. In the theoretical portion of this thesis, the relationship used was $\sqrt{c\,\delta\mathbf{d}^T\mathbf{A}\delta\mathbf{d} + b\,\delta\lambda^2} = \delta a$, discussed in Section A.2. Augmenting the equilibrium equations with this constraint results in a system that never becomes singular, as shown in [13]. The solution can pass critical points without loss of stability and follow the true equilibrium path since no assumptions about the response have been made. Bifurcation points can be identified and followed in a controlled manner.

Adapting arc length control for an experimental system is more difficult than load and displacement control. The formulation of the arc length constraint used in a finite element solver is not suitable as an experimental controller. Numerically, displacements can be imposed separately and the difference between internal and applied loads can be calculated. Experimentally, most experiment are conducted with displacement control, with no direct control over load. The structure must always be in equilibrium, so no residual between internal and external forces exists. Displacement and load are coupled through the structure, so one can be taken as a dependent variable.

Considering the experimental setup discussed in this chapter, a controller can be derived. The constraints on the system are (1) the side actuators are at zero load at an equilibrium configuration and (2) the arc length constraint must be satisfied. Each actuator can be controlled directly, so the three displacements will be used as the degrees of freedom. Loads can be measured for determining constraint satisfaction. The three constraints in equation form are

$$F_1(d_1, d_2, d_3) = 0, \tag{3.1}$$

$$F_3(d_1, d_2, d_3) = 0, \tag{3.2}$$

$$f(d_1, d_2, d_3, \lambda) = \delta a, \tag{3.3}$$

where $f(d_1, d_2, d_3, \lambda)$ is the function for the arc length constraint. The residuals for this system are $R_1 = -F_1$, $R_3 = -F_3$, and $\delta a - f$. Calculating the Jacobian of this system results in the 3 local equilibrium equations,

$$\begin{bmatrix} F_{1,1} & F_{1,2} & F_{1,3} \\ F_{3,1} & F_{3,2} & F_{3,3} \\ f_{,1} & f_{,2} & f_{,3} \end{bmatrix} \begin{bmatrix} \Delta d_1 \\ \Delta d_2 \\ \Delta d_3 \end{bmatrix} = \begin{bmatrix} R_1 \\ R_3 \\ \delta a - f \end{bmatrix}. \tag{3.4}$$

Conveniently, the first and second rows of Eq. 3.4 correspond to the first and third rows of the tangent stiffness matrix, and the third row is the partial derivative $\mathbf{f}_{,\mathbf{d}}$ discussed in Section A.2. As all of these values can be calculated experimentally, this appears to be a valid controller for an experimental system. Unfortunately, convergence could not be achieved while testing this formulation.

3.5 Hybrid Load/Displacement Control

Since arc length control was not successful, a more brute force approach had to be taken. Utilizing prior knowledge of the form of the snap-through response, a controller can be designed to stabilize a particular branch of the response. The first symmetric unstable branch of the snap-through response can be stabilized by three constraints, corresponding to the three actuators in the experiment. To match the load case of a central point load, the two side actuators are constrained to carry no load. The displacement of the central actuator was incrementally increased, since a majority of the symmetric branch was monotonic, up until a displacement tangency. The resulting control system used displacement control on the central actuator and load control on the side actuators. The tangent stiffness at each iteration was approximated with the secant stiffness. Each actuator was moved a small amount, and the change in load was measured. Dividing that change by the small displacement gave a column of the stiffness matrix.

This system has some significant pros and cons. The limitations of both numerical methods are present in this hybrid system; the system is only stable between critical points and will switch to a lower energy solution branch when a displacement tangency is reached. The calculation of the tangent stiffness is slow. Convergence criteria must be tuned to the error of the measurement devices used. However, this system can be expanded to stabilize any arbitrary branch. Higher energy branches require more constraints, which is not a problem for a Newton-Raphson scheme. Lower energy branches can be followed as well, but the starting point must be chosen to avoid critical points.

3.6 Control System Implementation

The experimental control system was implemented in LabVIEW 2016. The load cells and actuators all utilized analog voltage for inputs and outputs. Three analog outputs were used to set the actuator stroke, and six analog inputs were used to read the load cells and actuator feedback. Two power supplies were used to power the components, as different voltages were needed.

A series of subroutines were developed to simplify development of the final control system. The lowest level routines translated voltages to load and displacement. Control routines for the actuators handled the feedback loop needed to move them accurately. Self-contained operations like calculating the tangent stiffness matrix were also packaged. By having these separate routines, more focus was put on the actual control system and less on the individual components.

The high-level flowchart for the control system is shown in Fig. 3.5. The inner loop is a Newton-Raphson (NR) load control loop on the side actuators, and the outer loop incrementally increases the displacement of the center actuator. A modification to the numerical NR scheme had to be made to account for experimental error. The residual had to be read multiple times per iteration because it would change every time the actuators moved. The actuators would never return to the exact same position and joint friction affected rotations. This became apparent when, after calculating the tangent stiffness, the displacement increment calculated from the residual did not decrease the load. Recalculating the residual before every use fixed this problem.

The accuracy of the components directly affected the efficiency of this control system. The control system took about two hours to converge on the results presented in Ch. 4, needing constant manual intervention. As the components were being operated near their precision limit, noise and natural scatter would cause bad readings. The most significant was bad tangent stiffness estimates. Bad predictions would drastically increase the residual, increasing the number of iterations. Some of the predictions would cause significant damage to the specimen and boundary support components, necessitating manual approval of each increment. When the system diverged, it had to be stopped and restarted from the last converged point. Components with higher accuracy would prevent many of these problems.

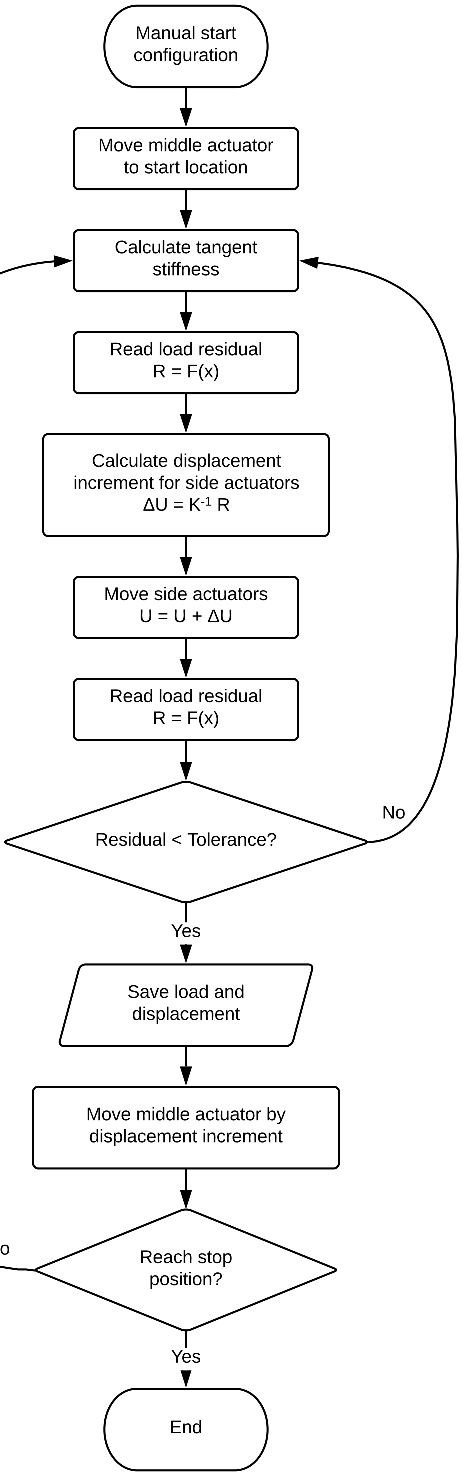

Figure 3.5: Flowchart of hybrid experimental control system for stabilization of unstable buckled configurations

Chapter 4

Experimental Results

4.1 Stabilized Branches for Centrally-Loaded Beam

An experiment was conducted to validate the stabilization predictions for a buckled beam. As previously mentioned, the beam had pin-pin boundary conditions and was loaded at the midpoint. LabVIEW was used to run the control system and collect data.

The force-displacement plot in Fig. 4.1 shows two distinct static equilibrium curves. The stable and asymmetric branches were obtained simultaneously using one control point under displacement control, and the symmetric branch was obtained using the hybrid control system. In the stable region, the structure takes a unique displaced shape. In this system, the bifurcation point occurs before the limit point. Since the control system was not able to converge around limit points, a gap in test data is present between midpoint displacements of -10mm and -7mm on the symmetric branch. The symmetric branch ends when the control system is no longer able to converge on a symmetric displaced shape, around a midpoint displacement of 4mm. The skew seen in the data is a result of asymmetries in the setup that could not be mitigated, such as flexibility of the hinges and residual friction in the ball-and-socket joints.

To illustrate the difference between the two paths, the displaced shape at a midpoint displacement of -0.75mm on both branches is shown in Fig. 4.2. The upper photo clearly

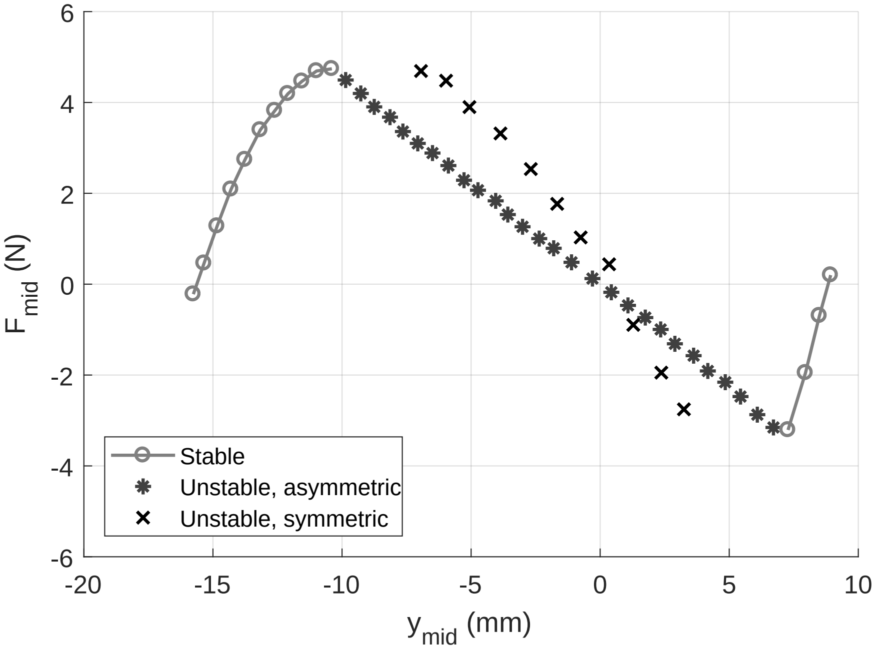

Figure 4.1: Force-displacement curve for the quasi-static snap-through response of a buckled beam under transverse loading

shows an asymmetric displaced shape, while the lower shows a symmetric shape. The asymmetric shape is stable under single-actuator control, while the symmetric requires at least two to stabilize. To reiterate, the two actuators on the sides are not carrying any load in this equilibrium configuration. Their presence prevents the structure from assuming the displaced shape of the upper photo.

As predicted, the three constraints used in this experiment were able to stabilize points along the second asymmetric branch as well, as seen in Fig. 4.3. Like in Fig. 4.2, the side actuators are not carrying any load, meaning this must be an equilibrium configuration along the second bifurcated branch of the force-displacement curve. Together, these experimental results show that experimental stabilization of higher snap-through buckling modes is a practical undertaking and sheds light on possible applications for other structures.

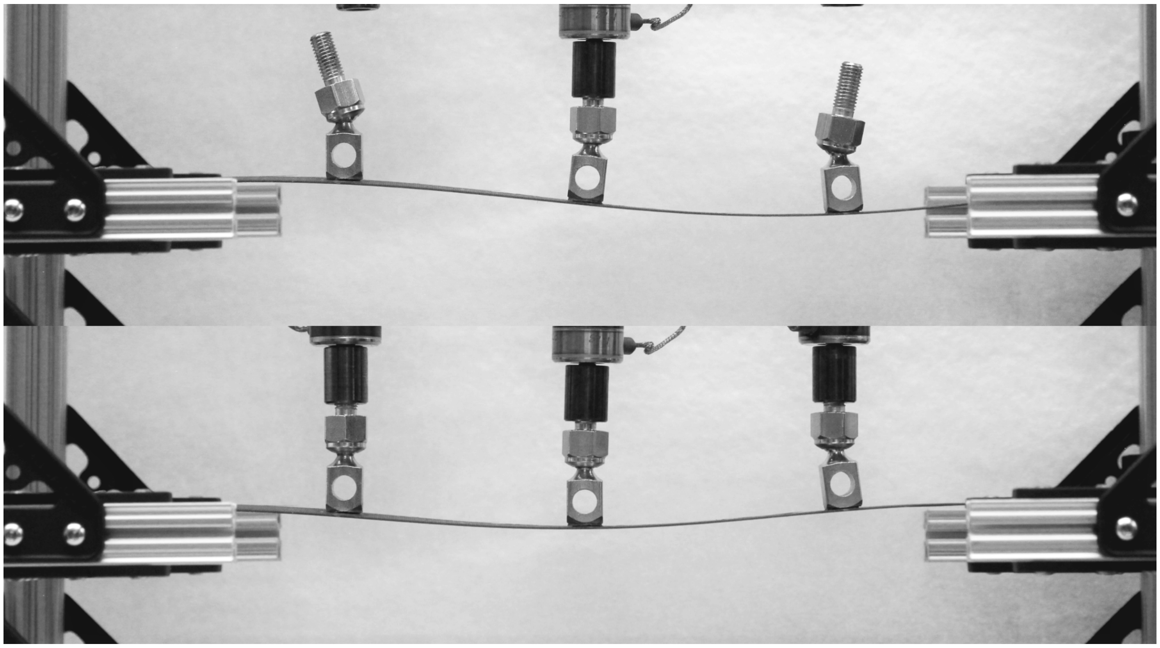

Figure 4.2: Displaced shapes at y_{mid} = -0.75mm, first asymmetric branch using one control point (upper photo), second symmetric branch using three control points (lower photo)

4.2 In-Class Demonstrations

With an experimental setup available, a number of in-class demonstrations were conducted. The direct stiffness method is widely used in structural engineering and thus is a large component of the undergraduate curriculum. The most common explanations rely on drawn diagrams and hand gestures to suggest moving an individual degree of freedom. Since the drawing does not respond to gestures, visualizing how the structure deforms can be a challenge. Flexible sticks work well showing how a single beam element responds to an imposed deformation, but demonstrations with multiple degrees of freedom are nearly impossible manually. This load frame enables more complicated demonstrations using multiple degrees of freedom and numerical results. The derivation and results for two demonstrations are detailed in the following sections.

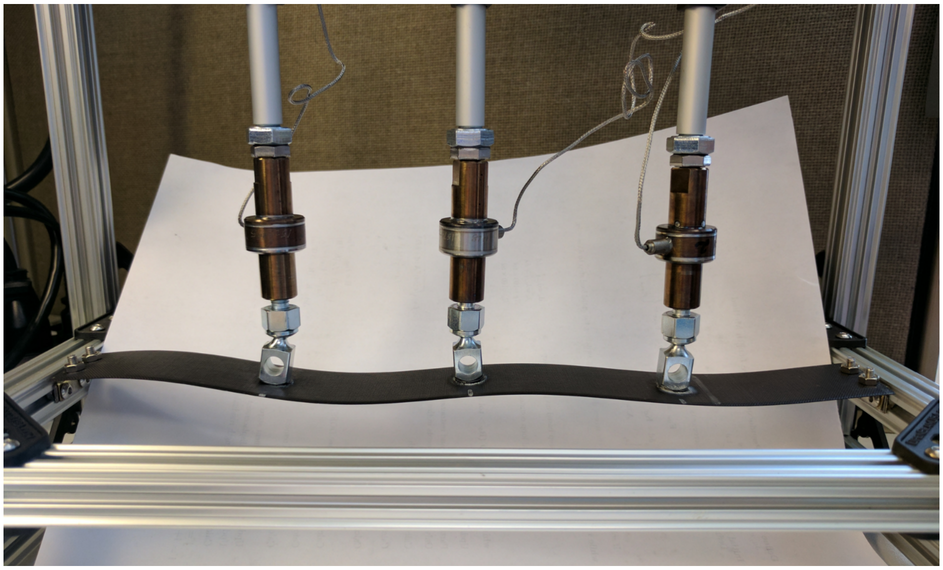

Figure 4.3: Stabilized equilibrium configuration along the second asymmetric branch

4.2.1 Three Point Bending Demonstration

When discussing Euler beam theory, the basics of the stiffness method are often introduced. A common derivation is the deflection of a simply supported beam due to a midspan point load, also referred to as three point bending. Starting with the governing differential equation and a moment diagram, a function for the displacement in terms of applied load can be derived. Inverting gives an equation in the form of $F = K\,u$. Given the material properties for a beam and two points on the force-displacement curve, the theoretical and experimental results can be compared. The following derivation was presented in a lecture for the University of Washington CEE 456-Structural Analysis class, along with results from the in-class demonstration.

$$M = EIv''$$

$$M = \begin{cases} \frac{PL}{4}\left(\frac{x}{L/2}\right) & x < \frac{L}{2} \\ \frac{PL}{2} - \frac{Px}{2} & x > \frac{L}{2} \end{cases}$$

$$v'' = \frac{M}{EI}$$

$$v'' = \begin{cases} \frac{PL}{4EI}\left(\frac{x}{L/2}\right) & x < \frac{L}{2} \\ \frac{PL}{2EI} - \frac{Px}{2EI} & x > \frac{L}{2} \end{cases}$$

$$v' = \begin{cases} \frac{Px^2}{4EI} + C_1 & x < \frac{L}{2} \\ -\frac{Px^2}{4EI} + \frac{PLx}{2EI} + D_1 & x > \frac{L}{2} \end{cases}$$

$$v = \begin{cases} \frac{Px^3}{12EI} + C_1x + C_2 & x < \frac{L}{2} \\ -\frac{Px^3}{12EI} + \frac{PLx^2}{4EI} + D_1x + D_2 & x > \frac{L}{2} \end{cases}$$

Using boundary and continuity conditions, solve for unknown constants.

$$v'\left(\frac{L}{2}\right) = \frac{PL^2}{16EI} + C_1 = -\frac{PL^2}{16EI} + \frac{PL^2}{4EI} + D_1 \Rightarrow C_1 = \frac{PL^2}{8EI} + D_1$$

$$v\left(0\right) = 0 \Rightarrow C_2 = 0$$

$$v\left(L\right) = -\frac{PL^3}{12EI} + \frac{PL^3}{4EI} + C_1L - \frac{PL^3}{8EI} + D_2 \Rightarrow D_2 = -\frac{PL^3}{24EI} - C_1L$$

$$\begin{aligned} v\left(\frac{L}{2}\right) &= \frac{PL^3}{96EI} + C_1\frac{L}{2} \\ &= -\frac{PL^3}{96EI} + \frac{PL^3}{16EI} + C_1\frac{L}{2} - \frac{PL^3}{16EI} - \frac{PL^3}{24EI} - C_1L \Rightarrow C_1 = -\frac{PL^2}{16EI} \end{aligned}$$

After plugging in values for C_1 and C_2 into v, find $v(L/2)$. Rearrange to find the expression for K.

$$\begin{aligned} v\left(L/2\right) &= \frac{PL^3}{96EI} - \frac{PL^3}{32EI} = -\frac{PL^3}{48EI} = -\delta \\ P &= \frac{48EI}{L^3}\delta \Rightarrow \mathbf{K} = \frac{\mathbf{48EI}}{\mathbf{L^3}} \end{aligned}$$

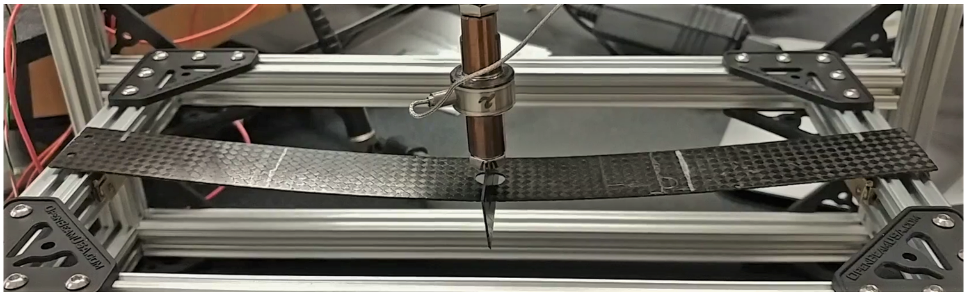

(a) Experimental three point bending test on a carbon fiber beam

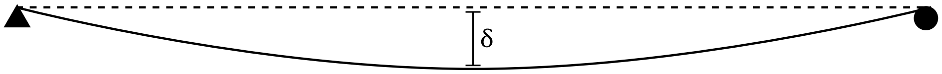

(b) Displaced shape during three point bending test

Figure 4.4: Three point bending test to determine stiffness coefficient

Table 4.1: Three Point Bending Stiffness Demonstration Values

Length, L (in)	9.25
Moment of Inertia, I (in^4)	4.11×10^{-6}
Young's Modulus, E (ksi)	2233.58
Measurement Point 1	$(0.9\,in, -0.025\,lb)$
Measurement Point 2	$(1.2\,in, 1.35\,lb)$

The demonstration was conducted with the beam detailed in Table 4.1. Using two points on the force-displacement curve. To finish the demonstration, the theoretical and experimental stiffnesses were calculated. There is only a 4% difference between the values, showing the accuracy of Euler-Bernoulli beam theory in a concise demonstration.

$$\mathbf{K}_{th} = \frac{48EI}{L^3} = \frac{48(2233.58*1000)(4.11 \times 10^{-6})}{(9.25)^3}\frac{lb}{in} = 0.557\,\frac{lb}{in}$$
$$\mathbf{K}_{exp} = \frac{P_2 - P_1}{\Delta_2 - \Delta_1} = \frac{0.135-(-0.025)}{1.2-.9}\frac{lb}{in} = 0.533\,\frac{lb}{in}$$

4.2.2 Condensed Stiffness Matrix Demonstration

Another important topic in structural analysis and structural dynamics is static condensation. In some cases, solving for the displacements or forces at some degrees of freedom is not necessary. Solving a reduced system is more efficient in these cases. The values that were condensed out can be recovered during post-processing. In the following example, the transverse stiffness of a beam discretized into four elements is desired. The ends are fixed and rotations are unrestrained but not measured at the free nodes. Only transverse loads will be applied to this beam. The effect of rotation on the transverse stiffness cannot be neglected, so the reduced system must still behave equivalently to the original system. Static condensation is the method used to reduce the system in this way.

A diagram detailing the boundary conditions and element discretization is shown in Fig. 4.5. Assuming every element has the same material properties and length, the following derivation gives the condensed stiffness matrix for the transverse degrees of freedom.

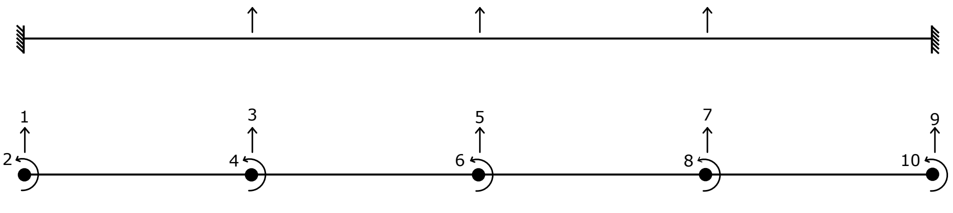

Figure 4.5: Boundary conditions and node numbering for a four element mesh to illustrate static condensation

$$\mathbf{K}_{el} = EI \begin{bmatrix} 12/L^3 & 6/L^2 & -12/L^3 & 6/L^2 \\ 6/L^2 & 4/L & -6/L^2 & 2/L \\ -12/L^3 & -6/L^2 & 12/L^3 & -6/L^2 \\ 6/L^2 & 2/L & -6/L^2 & 4/L \end{bmatrix} = \begin{bmatrix} \mathbf{K}_{11} & \mathbf{K}_{12} \\ \mathbf{K}_{21} & \mathbf{K}_{22} \end{bmatrix}$$

$$\mathbf{K}_{global} = \begin{bmatrix} \mathbf{K}_{11} & \mathbf{K}_{12} & \mathbf{0} & \mathbf{0} & \mathbf{0} \\ \mathbf{K}_{21} & \mathbf{K}_{22}+\mathbf{K}_{11} & \mathbf{K}_{12} & \mathbf{0} & \mathbf{0} \\ \mathbf{0} & \mathbf{K}_{21} & \mathbf{K}_{22}+\mathbf{K}_{11} & \mathbf{K}_{12} & \mathbf{0} \\ \mathbf{0} & \mathbf{0} & \mathbf{K}_{21} & \mathbf{K}_{22}+\mathbf{K}_{11} & \mathbf{K}_{12} \\ \mathbf{0} & \mathbf{0} & \mathbf{0} & \mathbf{K}_{21} & \mathbf{K}_{22} \end{bmatrix}_{10x10}$$

The degrees of freedom can be grouped as follows: translational-(3,5,7), rotational-(2,4,6), fixed-(1,2,9,10). Working with the free degrees of freedom, the system can be partitioned into translational and rotational degrees of freedom.

$$\begin{bmatrix} \mathbf{K}_{tt} & \mathbf{K}_{tr} \\ \mathbf{K}_{rt} & \mathbf{K}_{rr} \end{bmatrix} \begin{Bmatrix} \mathbf{u}_t \\ \mathbf{u}_r \end{Bmatrix} = \begin{Bmatrix} \mathbf{F}_t \\ \mathbf{F}_r \end{Bmatrix}$$

Since no moments are applied, or $\mathbf{F}_r = 0$, then the rotations can be expressed in terms of the translations. Substitution leads to an equation for the condensed stiffness.

$$
\begin{aligned}
\mathbf{K}_{tt}\mathbf{u}_t + \mathbf{K}_{tr}\mathbf{u}_r &= \mathbf{F}_t \\
\mathbf{K}_{rt}\mathbf{u}_t + \mathbf{K}_{rr}\mathbf{u}_r &= \mathbf{0} \\
\mathbf{u}_r &= \mathbf{K}_{rr}^{-1}\mathbf{K}_{rt}\mathbf{u}_t \\
\mathbf{K}_{tt}\mathbf{u}_t + \mathbf{K}_{tr}\mathbf{K}_{rr}^{-1}\mathbf{K}_{rt}\mathbf{u}_t &= \mathbf{F}_t \\
\left(\mathbf{K}_{tt} - \mathbf{K}_{tr}\mathbf{K}_{rr}^{-1}\mathbf{K}_{rt}\right)\mathbf{u}_t &= \mathbf{F}_t \\
\mathbf{K}_{cond} &= \mathbf{K}_{tt} - \mathbf{K}_{tr}\mathbf{K}_{rr}^{-1}\mathbf{K}_{rt}
\end{aligned}
$$

Carrying out this calculation gives the 3x3 matrix relating the translational degrees of freedom to concentrated transverse loads for this problem.

$$
\mathbf{K}_{cond} = \frac{EI}{L^3}\begin{bmatrix} 132/7 & -12 & 36/7 \\ -12 & 15 & -12 \\ 36/7 & -12 & 132/7 \end{bmatrix} \approx \frac{EI}{L^3}\begin{bmatrix} 18.9 & -12 & 5.14 \\ -12 & 15 & -12 \\ 5.14 & -12 & 18.9 \end{bmatrix}
$$

The tangent stiffness can be approximated using the secant stiffness in a physical demo. To obtain a column of the stiffness matrix, move the corresponding actuator a small amount, measure the change in transverse load at all three nodes, and divide the change in force by the change in displacement. Doing this three times, once for each transverse degree of freedom, gives the condensed stiffness matrix derived above. Figure 4.6 shows the displaced shape of the beam with the first node moved by 0.1 in. The resulting stiffness matrix from the demonstration is given below.

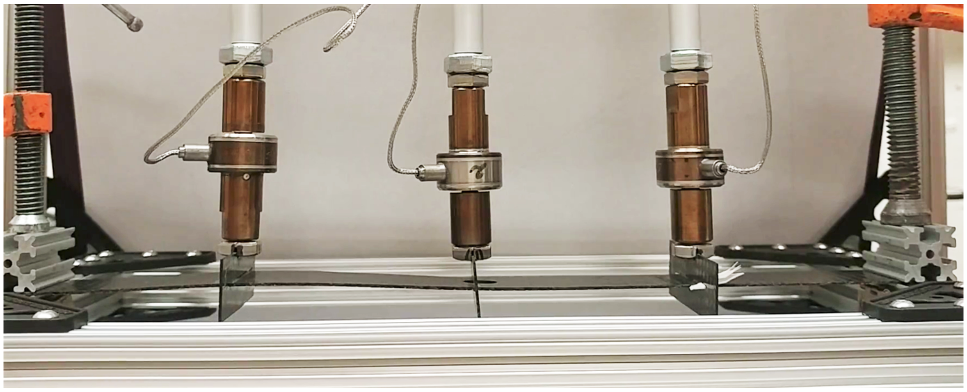

(a) Displacing one node of a beam to find a column of the experimental stiffness matrix

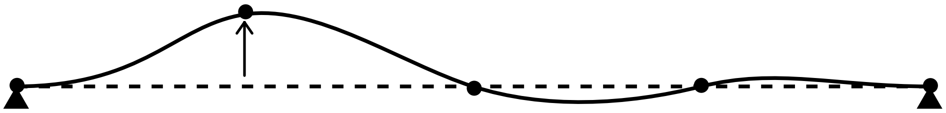

(b) Displaced shape after moving one node, exaggerated

Figure 4.6: Experimental determination of condensed stiffness matrix using unit displacement method

$$\mathbf{K}_{exp} = \begin{bmatrix} 29.06 & -5.66 & 2.4 \\ -14.67 & 9.6 & -14.05 \\ 3.22 & -9.08 & 29.55 \end{bmatrix} \frac{lb}{in}$$

A few useful conclusions can be drawn from the results. This test shows the unit displacement method for finding the stiffness in a way that hand gestures and drawings cannot. The resulting stiffness matrix is a similar form to the theoretical. No experiment will agree perfectly, but the qualitative agreement is good. Comparing the relative magnitudes reveals a significant problem with the actuators. The experimental stiffness is not symmetric. As previously mentioned, the actuators have inherent backlash in their screw drives, allowing small movements even when stopped. When the middle actuator moved, the side actuators would move a small amount, leading to a lower measured change in load. Since the side actuators had a rigid support at one end, the results were more accurate and effectively equal. The relative stiffnesses within the first and third columns were problematic, however. The other two actuators would move small amounts, reducing the load transferred.

Chapter 5

Conclusion

5.1 Summary of Work

This thesis covered the conditions for stabilizing unstable equilibrium configurations and applied them to a class of buckled beams exhibiting snap-through buckling. A control system was designed with a combination of nonlinear solution methods to verify the predictions experimentally. In addition, two class demonstrations were conducted using the load frame and control system to illustrate stiffness method topics.

5.1.1 Stabilization Concepts

The idea to stabilize unstable force-displacement paths was inspired by the work in [3] stabilizing unstable steady-state dynamic response. Unstable equilibria would prefer to deform into a lower energy configuration, and they will do so in the form of the unstable buckling modes. By preventing movements in the unstable modes, a general structure can be stabilized in an arbitrary unstable equilibrium configuration.

The case of an initially flat buckled beam with pin boundary conditions under transverse loading was considered as a specific example. Using the observations that the unstable mode shapes for this structure take the form of the classic Euler buckling mode shapes, a set of optimal constraints that mitigate each mode was proposed. Numerical models were created to explore the sensitivity of the stability of the system to constraint location. For low buckled rises, the optimal constraint positions appear to line up with the nodes of the Euler buckling mode shapes, though the stability of lower energy branches is less sensitive to constraint position than the desired branch. The lack of closed-form equation for the response and complex interaction between nodal constraints and modal response leaves no clear way to prove this conclusively.

5.1.2 Experimental Applications

To test these predictions, an experimental control system was developed to stabilize an unstable equilibrium branch of a buckled beam. Using the arc length method as the basis of the control system was not successful, but the formulation looks promising. By creating a hybrid control system utilizing both load and displacement control, portions of an unstable branch were successfully stabilized, demonstrating the theoretical predictions. Points along a higher energy branch were also stabilized manually to explore the full range of possible stable configurations.

5.1.3 Class Demonstrations

The load frame and control system were also utilized for in-class demonstrations on the stiffness method in structural analysis classes. The first demonstration was for an undergraduate introduction to structural analysis, estimating the stiffness coefficient for a beam under three point bending. The theoretical stiffness was found by solving the governing differential equation and plugging in the proper material properties and compared to the experimental stiffness found by calculating the slope of the force-displacement curve. The second demonstration used multiple actuators to show how to derive a stiffness matrix using unit displacements and use static condensation to reduce the order of the system. This demonstration worked well as a qualitative demonstration, but imperfections in the experimental setup prevented close agreement in the results.

Both demonstrations were well received by the students. The demonstrations were more effective at illustrating these topics than drawings or hand gestures. The flexibility and portability of the load frame enabled quick setup and immediate experimental feedback. Given the success, more will be conducted in the future.

5.2 Future Work

5.2.1 Stabilization Concepts

This thesis only discussed the stabilization for transverse loading of buckled beams with pin boundary conditions. The conclusions were based on observations rather than a rigorous solution, so further theoretical analysis is necessary. One assumption made is that stabilizing an Euler buckling mode will guarantee the stability of all lower modes. Another topic needing further study is determining how much of a branch can be stabilized by a given constraint set. This stabilization process can be carried out for any unstable structure and loading combination, each with their own challenges and interesting results. Two logical extensions of this research would be applying fixed end boundary conditions rather than pin and applying multi-parameter loading. More complex structures such as buckled plates could be of more practical interest.

5.2.2 Experimental Applications

This topic would benefit greatly from more experimental work. An experimental setup with higher resolution equipment or a larger scale would provide better convergence of the control system. New load cases, boundary conditions, and structural classes need to be studied to determine their stabilization criteria. In addition, there are few practical applications for this research, but the rise of microelectromechanical systems (MEMS) and snap-through buckling of aerospace structures may provide new opportunities to apply this research.

From a control system standpoint, the hybrid method used in this thesis had a few clear limitations. A formulation based on the arc length method was proposed, but it requires further work to determine its viability. Given the wealth of nonlinear numerical methods that exist, there are many avenues for research related to experimentation with multiple degrees of freedom.

Bibliography

[1] Jan Sieber and Bernd Krauskopf. Control based bifurcation analysis for experiments. *Nonlinear Dynamics*, 51(3):365–377, 2008.

[2] Jan Sieber, Alicia Gonzalez-Buelga, SA Neild, DJ Wagg, and Bernd Krauskopf. Experimental continuation of periodic orbits through a fold. *Physical review letters*, 100(24):244101, 2008.

[3] David AW Barton and Stephen G Burrow. Numerical continuation in a physical experiment: investigation of a nonlinear energy harvester. *Journal of Computational and Nonlinear Dynamics*, 6(1):011010, 2011.

[4] E Riks. An incremental approach to the solution of snapping and buckling problems. *International Journal of Solids and Structures*, 15(7):529–551, 1979.

[5] MA Crisfield. A fast incremental/iterative solution procedure that handles snap-through. *Computers & Structures*, 13(1-3):55–62, 1981.

[6] YC Fung and A Kaplan. Buckling of low arches or curved beams of small curvature. Technical report, NACA, 1952.

[7] Jen-San Chen and Shao-Yu Hung. Snapping of an elastica under various loading mechanisms. *European Journal of Mechanics-A/Solids*, 30(4):525–531, 2011.

[8] PS Harvey and LN Virgin. Coexisting equilibria and stability of a shallow arch: Unilateral displacement-control experiments and theory. *International Journal of Solids and Structures*, 54:1–11, 2015.

[9] B Camescasse, A Fernandes, and J Pouget. Bistable buckled beam and force actuation: Experimental validations. *International Journal of Solids and Structures*, 51(9):1750–1757, 2014.

[10] Herzl Chai. The post-buckling response of a bi-laterally constrained column. *Journal of the Mechanics and Physics of Solids*, 46(7):11551161–11591181, 1998.

[11] R Wiebe and LN Virgin. On the experimental identification of unstable static equilibria. In *Proc. R. Soc. A*, volume 472, page 20160172. The Royal Society, 2016.

[12] Mihaela Nistor, Richard Wiebe, and Ilinca Stanciulescu. Relationship between euler buckling and unstable equilibria of buckled beams. *International Journal of Non-Linear Mechanics*, 95:151–161, 2017.

[13] Richard Wiebe. *Nonlinear dynamics of discrete and continuous mechanical systems with snap-through instabilities.* PhD thesis, Duke University, 2012.

[14] Garrett Hall and Eric Kasper. Lecture notes in an introduction to matrix structural analysis, September 2015.

Appendix A

Numerical Methods

A.1 Overview

This appendix covers the formulation and implementation of the nonlinear FEM code used in this project. Because of the highly nonlinear response of structures exhibiting snap-through buckling, the arc-length solution method was used. This method was pioneered by Crisfield in [5] for structures that exhibit limit-point instabilities and snap-through buckling. The arc length formulation was originally presented in [13] and more details are provided here. The structure of the FEM code was based off the work of Dr. Hall and Dr. Kasper of Cal Poly San Luis Obispo presented in their CE501: Advanced Matrix Analysis of Structures class [14].

A.2 Formulation of Arc Length Method for FEA

For an elastic structure and conservative loading parameterized by a scalar λ, there exists a potential energy function $U(\mathbf{d}, \lambda)$. Equilibrium solutions to this function satisfy the relation

$$\nabla U(\mathbf{d}, \lambda) = 0.$$

This is the energy form of Newton's 2^{nd} law for a static system. Therefore, the sum of forces in the system can be represented as

$$\nabla U(\mathbf{d}, \lambda) = \mathcal{F}(\mathbf{d}, \lambda) = \mathbf{F_{int}}(\mathbf{d}) - \mathbf{F_{ext}}(\mathbf{d}, \lambda) = 0, \tag{A.1}$$

where the internal force vector $\mathbf{F_{int}}$ is a function of the system displacement $\mathbf{d}$ and the external force vector $\mathbf{F_{ext}}$ is a function of the load parameter λ and possibly $\mathbf{d}$, depending on the formulation. Note that this form is only valid for conservative loads and one parameter forcing. $\mathbf{F_{int}}$ is the gradient of the strain energy component of the total strain energy.

Given a non-equilibrium configuration $(\mathbf{d}, \lambda)$, which is typically an initial estimate, a $(\Delta\mathbf{d}, \Delta\lambda)$ is sought such that

$$\begin{aligned}\mathcal{F}(\mathbf{d} + \Delta\mathbf{d}, \lambda + \Delta\lambda) = \mathcal{F}(\mathbf{d}, \lambda) + \frac{\partial \mathcal{F}}{\partial \mathbf{d}}\Delta\mathbf{d} + \frac{\partial \mathcal{F}}{\partial \lambda}\Delta\lambda &= 0,\\ \mathcal{F}(\mathbf{d}, \lambda) + \mathbf{K_T}\Delta\mathbf{d} - \mathbf{F_{ext}}\Delta\lambda &= 0,\\ \mathbf{K_T}\Delta\mathbf{d} - \mathbf{F_{ext}}\Delta\lambda &= -\mathcal{F}(\mathbf{d}, \lambda).\end{aligned}$$

The tangent stiffness $\mathbf{K_T}$ and external force $\mathbf{F_{ext}}$ are evaluated at the current $(\mathbf{d}, \lambda)$ The load residual can be defined as $\mathbf{R} = -\mathcal{F}(\mathbf{d}, \lambda)$. Substituting this into the expression above gives the linearized expression for local equilibrium,

$$\mathbf{K_T}\Delta\mathbf{d} - \mathbf{F_{ext}}\Delta\lambda = \mathbf{R}. \tag{A.2}$$

A relationship between $\mathbf{\Delta d}$ and $\Delta\lambda$ is necessary to solve this equation. The arc length method derives its name from the use of variations on the arc length formula from calculus as this relationship. In [13], the constraint is given as

$$f(\delta\mathbf{d}, \delta\lambda) = \sqrt{c\,(\delta\mathbf{d})^T \mathbf{A}\,\delta\mathbf{d} + b\,\delta\lambda^2} = \delta a,$$

which defines an ellipsoid in the n+1 dimensional space of the problem. The vector $\delta\mathbf{d}$ and scalar $\delta\lambda$ are the changes in displacement and load from the last converged point. The arc length is given by the scalar δa. The scalar factors c and b are weighting terms that define the contribution of displacement and load in the constraint. The factor $\mathbf{A}$ is a scaling matrix on the displacement term to transform it into force-like units and magnitude. The form $\mathbf{A} = \mathbf{K_{T}}_0^T \mathbf{K_{T}}_0$ is selected for this derivation, where $\mathbf{K_{T}}_0$ is the tangent stiffness evaluated at the initial step. At the beginning of the analysis, δa, c, and b are set by the analyst, which will take some trial and error to refine. A rule of thumb for selecting c and b is to have $c + b = 1$, creating a simple weighting for how much the load or displacement increments control the analysis. The balance between c and b is subtle and varies from problem to problem, but setting $c = b = 0.5$ is a reasonable starting point. When choosing δa, start with something reasonable for the order of magnitude of the problem. If convergence is not achieved, simply decrease δa. Increase or decrease δa to adjust the distance between solution points as desired once converged. Linearizing the arc length constraint using the Taylor expansion and assuming $\mathbf{A}$ is symmetric,

$$\begin{aligned}
\delta a &= f(\delta\mathbf{d} + \Delta\mathbf{d}, \delta\lambda + \Delta\lambda),\\
\delta a &= f(\delta\mathbf{d}, \delta\lambda) + \frac{\partial f}{\partial \delta\mathbf{d}}\Delta\mathbf{d} + \frac{\partial f}{\partial \delta\lambda}\Delta\lambda,\\
\delta a &= f(\delta\mathbf{d}, \delta\lambda) + \frac{c}{f(\delta\mathbf{d}, \delta\lambda)}\frac{1}{2}\left(\delta\mathbf{d}^T \mathbf{A}\,\Delta\mathbf{d} + \Delta\mathbf{d}^T \mathbf{A}\,\delta\mathbf{d}\right) + \frac{b}{f(\delta\mathbf{d}, \delta\lambda)}\delta\lambda\,\Delta\lambda,\\
\delta a &= f(\delta\mathbf{d}, \delta\lambda) + \frac{c}{f(\delta\mathbf{d}, \delta\lambda)}(\delta\mathbf{d})^T \mathbf{A}\,\Delta\mathbf{d} + \frac{b}{f(\delta\mathbf{d}, \delta\lambda)}\delta\lambda\,\Delta\lambda.
\end{aligned}$$

The residual in the arc length is $\delta a - f(\delta\mathbf{d}, \delta\lambda)$. Rearranging terms in the linearized form of the arc length constraint results in

$$\frac{c}{f}(\delta\mathbf{d})^T \mathbf{A}\,\Delta\mathbf{d} + \frac{b}{f}\delta\lambda\,\Delta\lambda = \delta a - f, \tag{A.3}$$

where $f(\delta\mathbf{d},\delta\lambda)$ is shortened to f for brevity.

Combining A.2 and A.3, a system of n+1 equations for the local equilibrium about the deformed configuration is obtained. For brevity, $\mathbf{f}_{,\mathbf{d}} = \frac{c}{f}(\delta\mathbf{d})^T\mathbf{A}$ and $f_{,\lambda} = \frac{b}{f}\delta\lambda$.

$$\begin{bmatrix} \mathbf{K_T} & -\mathbf{F_{ext}} \\ \mathbf{f}_{,\mathbf{d}} & f_{,\lambda} \end{bmatrix} \begin{bmatrix} \Delta\mathbf{d} \\ \Delta\lambda \end{bmatrix} = \begin{bmatrix} \mathbf{R} \\ \delta a - f \end{bmatrix} \tag{A.4}$$

The augmented matrix is always positive definite for structural systems, even when $\mathbf{K_T}$ is singular. However, this augmented matrix does not retain many of the qualities that stiffness matrices do, such as narrow bandwidth and symmetry. It is possible to solve for $\mathbf{\Delta D}$ and $\Delta\lambda$ directly. It is also possible to decouple the system to retain numerical efficiency. This sacrifices numerical stability in the immediate vicinity of a singular point for the ability to use specialized matrix solvers. To begin decoupling, solve for $\Delta\mathbf{d}$ in A.2,

$$\Delta\mathbf{d} = \mathbf{K_T}^{-1}\left(\mathbf{R} + \mathbf{F_{ext}}\Delta\lambda\right),$$

and substitute the result into A.3. Solving for $\Delta\lambda$,

$$\mathbf{f}_{,\mathbf{d}}\left(\mathbf{K_T}^{-1}\mathbf{R} + \mathbf{K_T}^{-1}\mathbf{F_{ext}}\Delta\lambda\right) + f_{,\lambda}\Delta\lambda = \delta a - f,$$

$$\Delta\lambda = \frac{(\delta a - f) - \mathbf{f}_{,\mathbf{d}}\left(\mathbf{K_T}^{-1}\mathbf{R}\right)}{\mathbf{f}_{,\mathbf{d}}\left(\mathbf{K_T}^{-1}\mathbf{F_{ext}}\right) + f_{,\lambda}}. \tag{A.5}$$

and substituting the expression into the equation for $\mathbf{\Delta d}$ results in the optional decomposition used to solve A.4,

$$\Delta\mathbf{d} = \mathbf{K_T}^{-1}\left(\mathbf{R} + \mathbf{F_{ext}}\Delta\lambda\right). \tag{A.6}$$

Note that $\mathbf{f}_{,\mathbf{d}}$ is a row vector, so $\mathbf{f}_{,\mathbf{d}}\left(\mathbf{K_T}^{-1}\mathbf{R}\right)$ and $\mathbf{f}_{,\mathbf{d}}\left(\mathbf{K_T}^{-1}\mathbf{F_{ext}}\right)$ are scalars by matrix multiplication. Generally, solutions start from an unloaded and undeformed state, where $\mathbf{d}^0 = \mathbf{0}$, $\lambda^0 = 0$. If the initial state is nonzero, $\mathbf{d}^0$ and λ^0 can be set to the known displacement and load factor. This is useful in a multi-step solution, where the final state of one loading is the initial state of the next.

Initial steps $\delta\mathbf{d}^0$ and $\delta\lambda^0$ are needed to start the solution process. One method is to use the initial tangent stiffness and a small initial load with the same sign as the dominant direction of the applied loads. A suggestion is given below, where the sign on $\delta\lambda^0$ is selected to start the solution in the proper direction. This is derived from A.2 with $\mathbf{R} = 0$,

$$\begin{aligned}
\delta\lambda^0 &= \pm\delta a,\\
\delta\mathbf{d}^0 &= \delta\lambda^0\mathbf{K_{T}}_0^{-1}\mathbf{F_{ext}}.
\end{aligned}$$

Next, solve the augmented system of equations for $\Delta\mathbf{d}$ and $\Delta\lambda$. Evaluate the necessary terms in the augmented matrix at the current iteration,

$$\begin{aligned}
f &= f\left(\delta\mathbf{d}_i^n, \delta\lambda_i^n\right),\\
\mathbf{f}_{,\mathbf{d}} &= \mathbf{f}_{,\mathbf{d}}\left(\delta\mathbf{d}_i^n, \delta\lambda_i^n\right),\\
f_{,\lambda} &= f_{,\lambda}\left(\delta\mathbf{d}_i^n, \delta\lambda_i^n\right),\\
\mathbf{K_T} &= \mathbf{K_T}\left(\mathbf{d}^{n-1} + \delta\mathbf{d}_i^n\right),\\
\mathbf{R} &= (\lambda^{n-1} + \delta\lambda_i^n)\mathbf{F_{ext}} - \mathbf{F_{int}}\left(\mathbf{d}^{n-1} + \delta\mathbf{d}_i^n\right).
\end{aligned}$$

and substitute them into A.5 and A.6 to calculate the increments in displacement and load. In these equations, the superscripts refer to the step count and the subscripts refer to the iteration count. Update the step increment,

$$\delta\mathbf{d}_{i+1}^{n} = \delta\mathbf{d}_{i}^{n} + \Delta\mathbf{d},$$

$$\delta\lambda_{i+1}^{n} = \delta\lambda_{i}^{n} + \Delta\lambda,$$

and check convergence with updated values for $\mathbf{R}$ and f,

$$norm\left(\mathbf{R}\right) < \text{tolerance},$$

$$\delta a - f < \text{tolerance}.$$

If convergence is satisfied, store the result for the current step as shown,

$$\mathbf{d}^{n} = \mathbf{d}^{n-1} + \delta\mathbf{d}_{i+1}^{n},$$

$$\lambda^{n} = \lambda^{n-1} + \delta\lambda_{i+1}^{n}.$$

A.3 Nonlinear FEA Code

No complete closed-form solution exists for the snap-through behavior of buckled continuous beams, so finite element analysis is the best method of theoretical analysis. Many commercial FEA codes implement a version of the arc-length solver, but better flexibility, customization, and efficiency made custom code more useful.

Matlab was used to create the code because of familiarity and ease of use. The features deemed necessary were: a) force and displacement histories, b) internal strain energy, c) natural frequency analysis, d) bifurcation analysis with solver restarting, and e) multi-step solutions.

As an example, the process for analyzing a structure similar to those used in experiments will be considered. Starting with a flat, unloaded beam, the order of a typical analysis went as follows:

1. Axial load was applied until the buckled rise reached a desired height. The end with an axial load had a roller boundary condition, while the other had a pin.
2. Starting with the displaced shape at the end of the first step, a transverse load was applied at the central node until a stop condition occurred. Both ends had pin boundary conditions.
3. If desired, bifurcations points were identified.
4. Analysis was restarted from each of the bifurcation points. Pin boundary conditions were applied at both ends.

These four steps are shown in Fig. A.1. A flowchart of the code is shown in Fig. A.2.

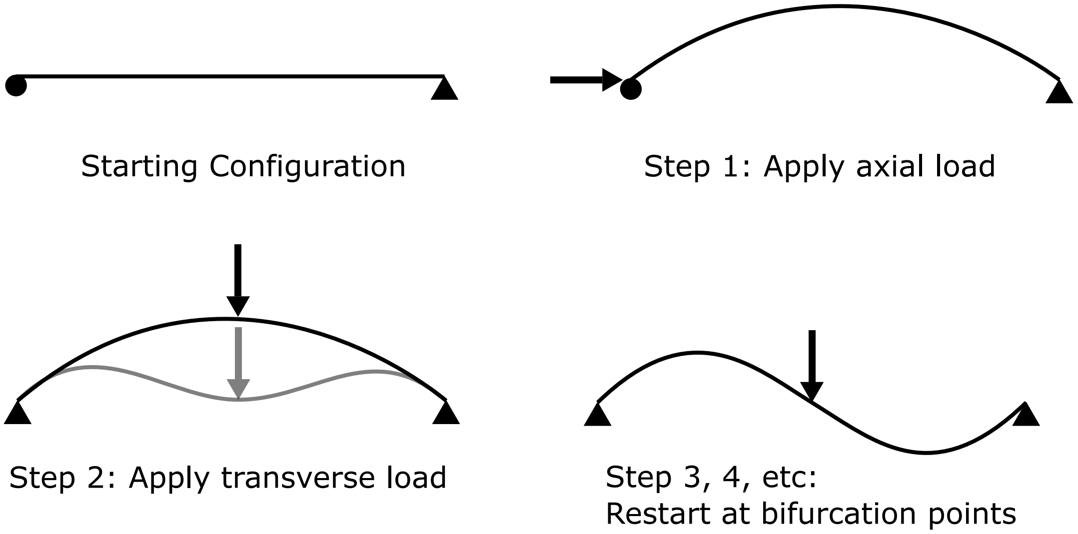

Figure A.1: Steps in analysis of snap-through beams

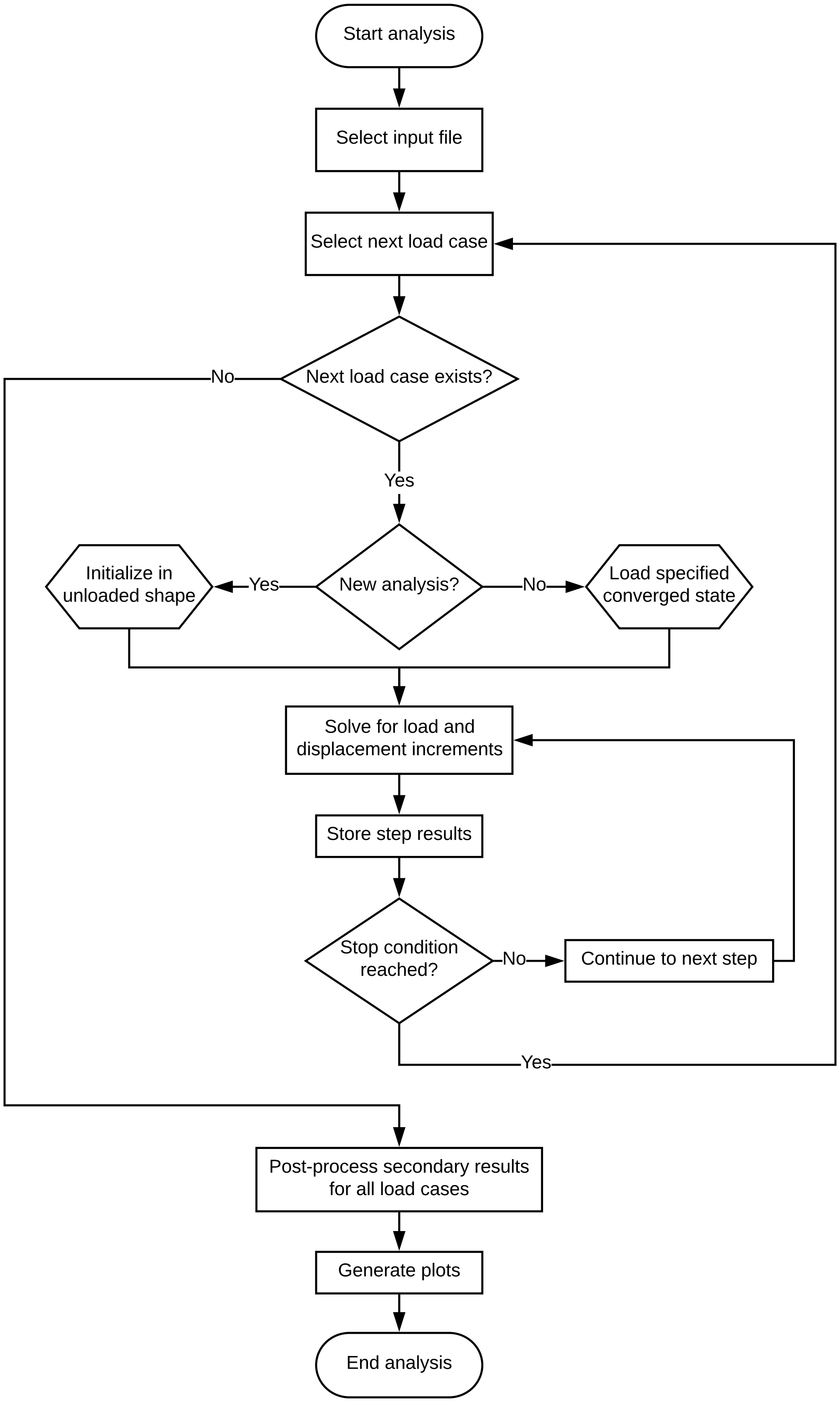

Figure A.2: Flowchart of multi-step nonlinear FEM package

A.4 Numerical Validation

This code has been validated using two methods. First, the numerical results are compared to the results presented in (cite Nistor Wiebe 2016) using the materials and dimensions in Table A.1. Second, experimental results on another beam are compared to a model with the same material properties and dimensions.

Table A.1: Beam Dimensions and Material Properties

Length, L (mm)	304.8
Cross-section area, A (mm^2)	0.32258
Moment of Inertia, I (mm^4)	0.1387438
Young's Modulus, E (GPa)	206.843
Density, ρ (kg/m^3)	1500

Fig. A.3 and Fig. A.4 show the code used in this project matches the results published in (cite Nistor 2016) for the nonlinear response of a buckled beam undergoing snap-through buckling. To obtain these curves, the point load was applied one node off from the center node. This is an analysis trick to avoid having to do a bifurcation analysis, as the analysis will go down all the bifurcation paths at the expense of missing the exact response in the vicinity of the bifurcation point.

Based on the presented results, the code developed for this research accurately predicts the response for beams exhibiting snap-through buckling for the elastic range of the material. It does not consider yielding, fracture, or failure.

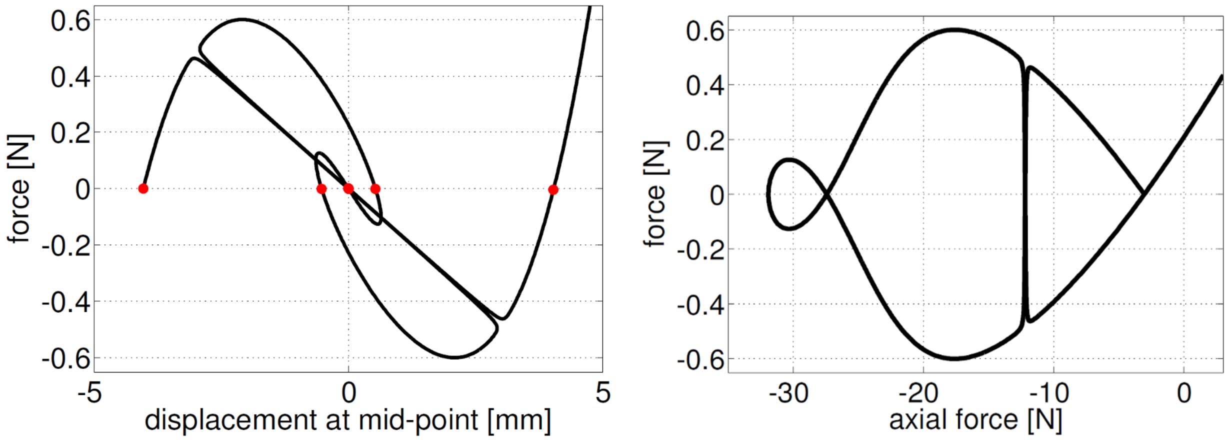

(a) Force-displacement (left) and axial force (right) plots for 4mm rise from Nistor 2016

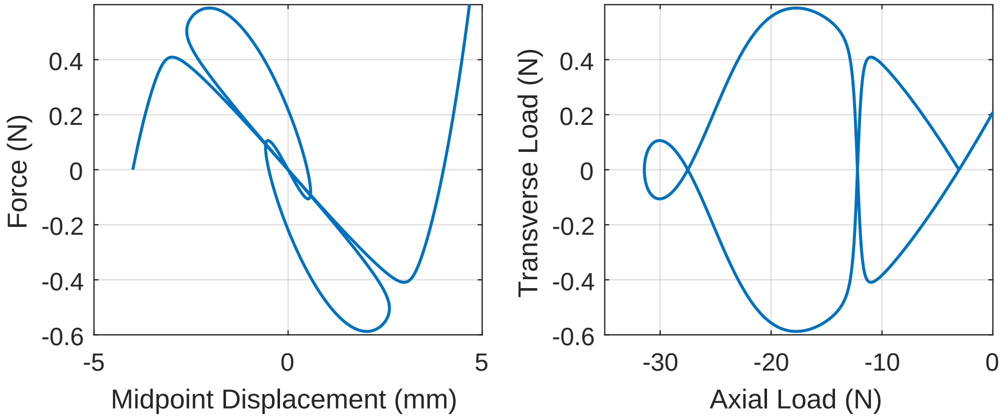

(b) Force-displacement (left) and axial force (right) plots for 4mm rise from current analysis

Figure A.3: Comparison of results for a 4mm rise between Nistor 2016 and current analysis

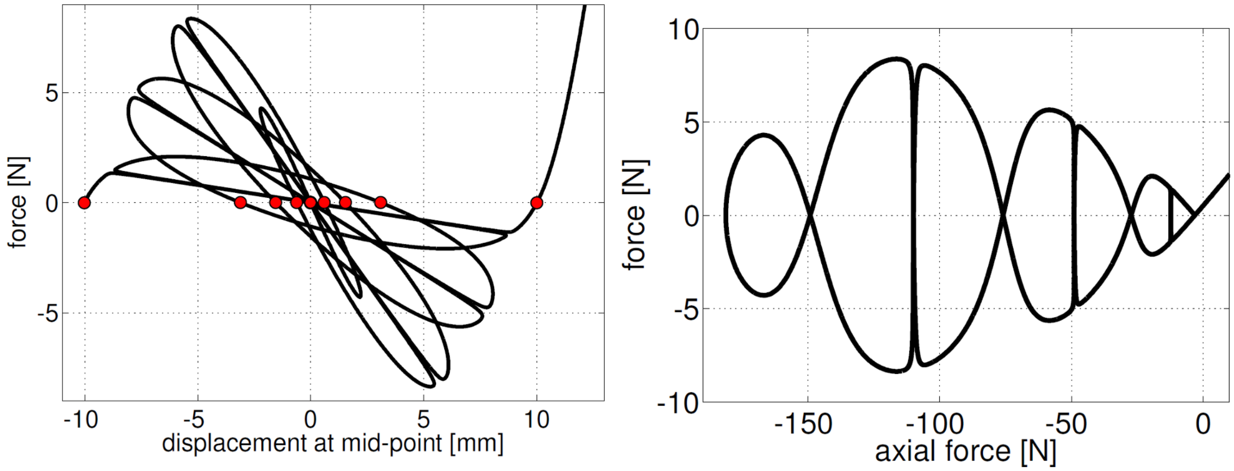

(a) Force-displacement (left) and axial force (right) plots for 10mm rise from Nistor 2016

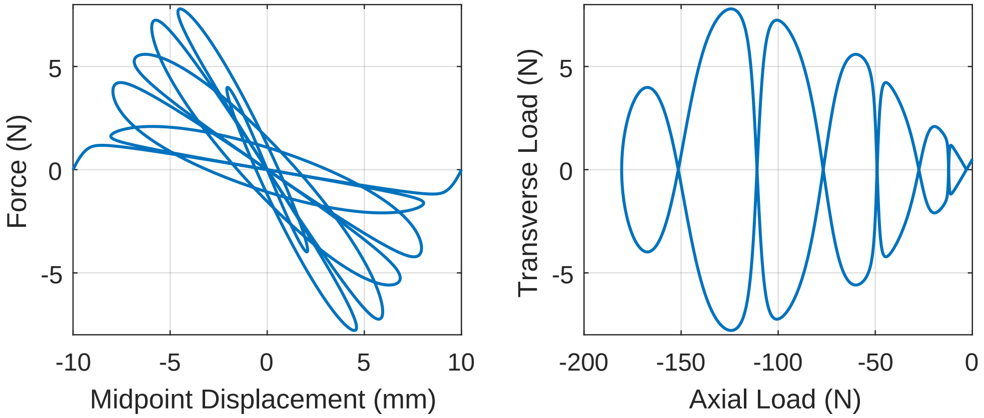

(b) Force-displacement (left) and axial force (right) plots for 10mm rise from current analysis

Figure A.4: Comparison of results for a 10mm rise between Nistor 2016 and current analysis

Appendix B

Ingraham High School Auditorium Analysis

This appendix covers additional work completed for Dr. Tyler Sprague, a professor in the Department of Architecture at the University of Washington. This work focused on identifying the buckling modes and failure states of a dome-like building that could exhibit bifurcations and snap-through response. Nonlinear analyses were not conducted, but many of the concepts from the primary research informed the conclusions of this case study. The development of a finite element model, the case studies considered and conclusions of the studies will be presented in this chapter.

Figure B.1: Auditorium at Ingraham High School, Seattle, WA

The structure under consideration is an auditorium at Ingraham High School in Seattle, WA, shown in Fig. B.1. It was constructed in the late 1950s, a time period where shell structures were popular for their ease of fabrication, simplified analysis, and architectural form. The reinforced concrete primary structure consists of three shells, each having a hyperbolic paraboloid shape and stiffened by ribs along the edges, visible in a construction photo in Fig. B.2. At the time period the building was designed, finite element methods were not widely available. Many shell structures of the same era do not have these stiffening ribs. To determine how critical the ribs are to the performance of the structure and the sensitivity to global architectural changes, modern finite element analysis tools were utilized.

Figure B.2: Construction photo of auditorium showing primary reinforced concrete structure

Using the construction plans, a 3D model was created using Solidworks, a parametric modeling program, shown in Fig. B.3. Nonstructural features such as walls and overhangs were neglected. Given the three-fold symmetry of the building, the model could be simplified into three components: (1) a hyperbolic paraboloid shell, (2) a central rib, and (3) an edge rib. Three shells, three central ribs, and six edge ribs made up the completed assembly. In addition, a model of the building without the ribs was created.

The study required modifications to the model geometry. The reference case was the as-built geometry, and any modifications scaled the entire structure or component uniformly. Abaqus/CAE, a commercial finite element program, was used to conduct the analysis.

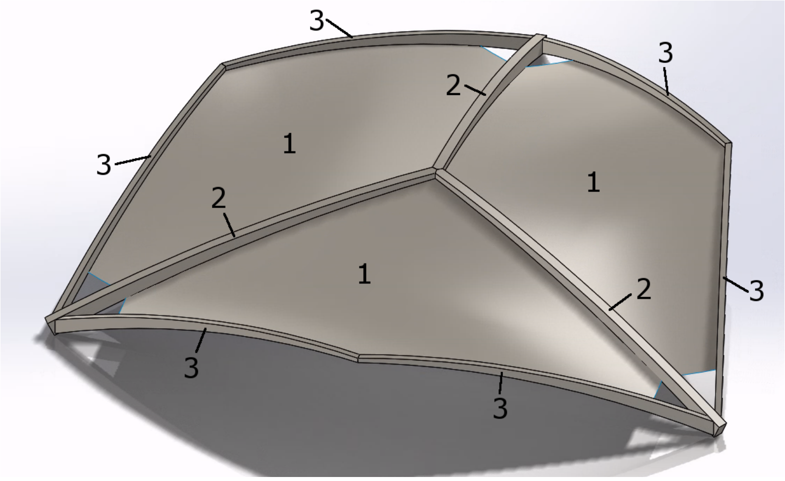

Figure B.3: 3D model of primary structure in Solidworks, labeled with (1) shells, (2) central ribs, and (3) edge ribs

The modeling assumptions are summarized in Table B.1. Since a linear model was being considered, gross section reinforced concrete properties were used. No rebar was modeled for simplicity. The yield strain of 60ksi steel was used as a cutoff for where the linear model was valid. The self-weight of the structure was applied as a dead load, and a uniform area live load was applied over the entire structure.

Table B.1: Auditorium Modeling Assumptions

Modulus of Elasticity, E (ksi)	4000
Poisson's Ratio, ν	0.2
Unit Weight (pcf)	140
Live Load (psf)	40
Failure Strain (in/in)	±0.002

All models were analyzed in the following fashion. First, the dead load was applied. Second, starting from the dead load deformed shape, a buckling calculation was conducted, scaling the live load until the first buckling load was reached. Third, starting from the dead load deformed shape, the live load was scaled until the shell's in-plane principal strain exceeded the failure strain anywhere in the structure. This results in two failure states, given by the load combinations $D + \lambda_B L$ and $D + \lambda_Y L$. The scaling factors λ_B and λ_Y are multipliers on the live load to reach the buckling and yielding failure states, respectively. They can also be viewed as a factor of safety on the structure's performance under the given live load. A scaling factor $\lambda = 2$ would mean the structure has been designed to a factor of safety of 2 for the considered loading.

Three design studies were considered to assess the sensitivity of the auditorium structure to global design parameters. These studies considered the depth of the ribs, the height of the structure, and the thickness of the shell. The modifications are given in Table B.2. Again, the percentage scaling was uniform, using the as-built as reference. The rib depth study examined the sensitivity of the as-built structure to rib depth. The height and shell thickness studies focused on the performance of just the shell, so ribs were not included. By comparing the as-built structure's performance to the height-thickness design space results, an equivalently performing shell structure without ribs could be found.

Table B.2: Design Study Parameters

	Study 1: Height	Study 2: Shell Thickness	Study 3: Rib Depth
Building Height (%)	70-130 by 10	100	100
Shell Thickness (in)	4, constant	2-6 by 0.5, constant	As-built (3-6)
Rib Depth (%)	No ribs	No ribs	0, 10, 25, 50, 75, 100

For the rib depth models, a mesh seed size of 5 inches was used. This ensured enough elements through the thickness of the ribs and good mesh compatibility between the shell and beams. For the height and shell thickness models, a mesh seed size of 15 was used. Tie constraints were used to couple the shell edges, beam-beam surfaces, and beam-shell surfaces. Fixed boundary conditions were applied at the ends of the central ribs, similar to the as-built condition. When no ribs were present, the edges of the shell nearest the ground were fixed instead. This is an approximation of how a shell-only structure would attach to the ground.

The buckling mode shapes for all analyses could be grouped into three modes: (1) global buckling, (2) local buckling, and (3) rib buckling. These groups can be seen in Fig. B.4. The expected causes for each buckling mode will be discussed with the design study results.

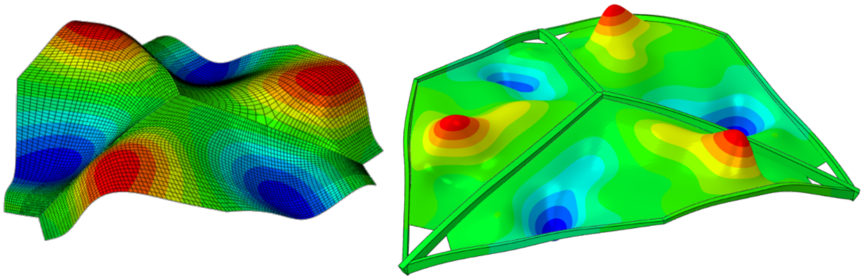

(a) Global Buckling, Mode 1

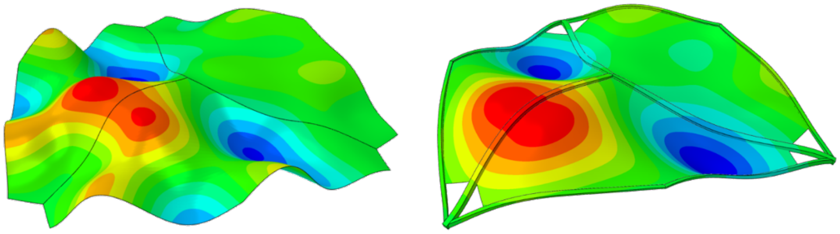

(b) Local Buckling, Mode 2

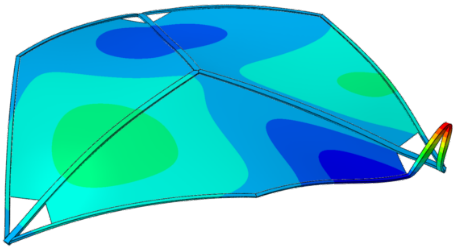

(c) Rib Buckling, Mode 3

Figure B.4: Typical buckling modes for all analysis results with and without ribs

Typical vertical displacement and in-plane principal strain plots are shown in Fig. B.5. The displacements that are present at the failure strain of 0.002 in/in are in the 6-9 inch range. At 2-3% of the building height, these are definitely into the realm of geometric nonlinearity. As will be seen, these occur at absurd load levels.

The results of the design study on rib depth are shown in Fig. B.6. This plot gives a direct comparison between the as-built structure and the shell without ribs. Because the live

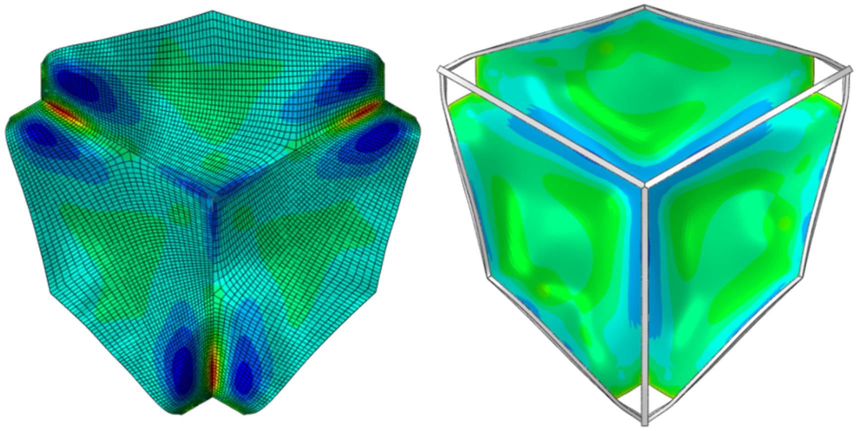

(a) Typical in-plane principal strain distribution

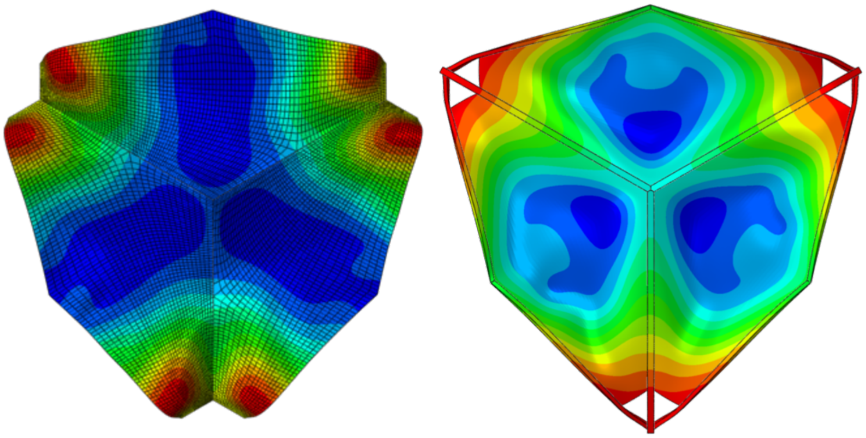

(b) Typical displaced shape

Figure B.5: Typical displaced shape and strain distribution for the design studies, with and without ribs, at a maximum strain of ±0.002 in/in

load multiplier is well above 1.0 for the no-rib case, the structure can carry the considered load adequately. For this load combination, the auditorium does not need the ribs. It performs equivalently to the case of 50% rib depth. For all cases, buckling failure occurs before material failure. The scaling factor for strain does not change appreciably for depths over 50%, so any additional thickness only increases the stiffness to prevent buckling. For small rib depths in the grayed region, the ribs buckle in a characteristic Euler buckling shape. For intermediate depths and for no ribs, the structure is able to buckle locally at the join between two shells, but this is prevented by the bending stiffness of the thicker ribs.

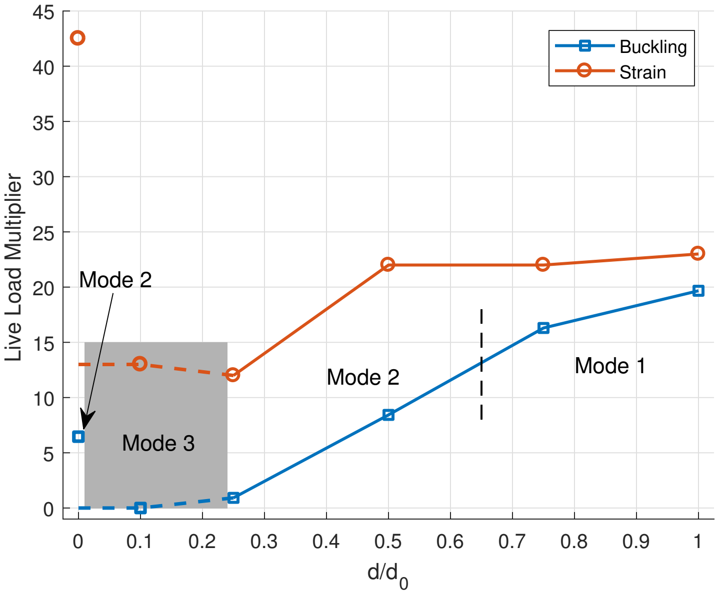

Figure B.6: Rib depth design study results, with buckling modes labeled

The results of the design study on shell height are shown in Fig. B.7. Again, buckling failure occurs before strain-controlled failure. The change in buckling mode is consistent with the trend seen in other types of arched structures. For low rises, a symmetric buckling mode manifests first. For higher rises, a larger component of the load is applied tangent to the shell, increasing membrane loads and causing a higher likelihood of local buckling in high compression regions. The curvature along the joins between individual hyperbolic paraboloids is quite strong, inducing P-Δ effects that induce buckling earlier. For structures with higher rises, asymmetric buckling modes are more energetically favorable.

The results of the design study on shell height are shown in Fig. B.8. Buckling failure again occurs before strain-controlled failure, but this time the order of the buckling modes is switched. Again, this is consistent with the order of buckling modes seen in other curved structures. For thinner shells, the resistance to out-of-plane bending is lessened. This increases the likelihood that the curvature of the structure will induce buckling. Thicker shells resist these rotations better, and at a certain point, localized buckling becomes less likely than a global buckling failure. Only at its thinnest is the structure susceptible to failure.

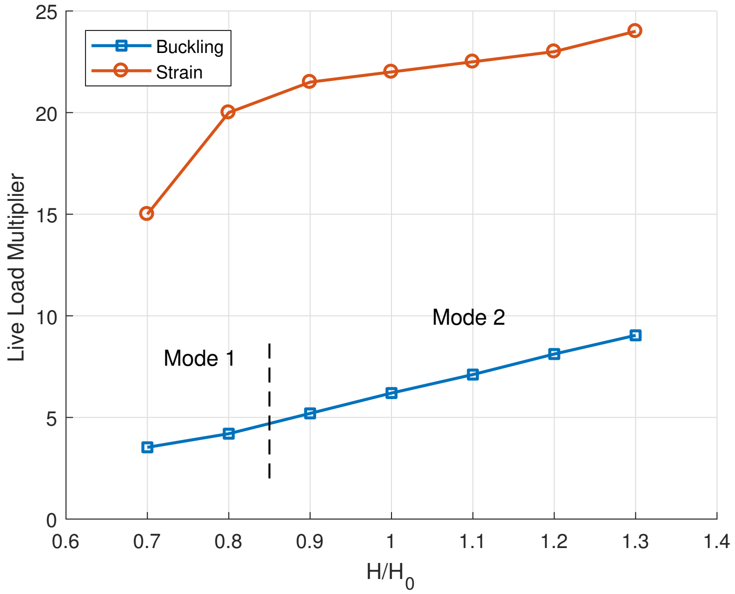

Figure B.7: Rise design study results, with buckling modes labeled

With the results of the design studies, three important conclusions can be drawn. First, the ribs on the auditorium appear to be a conservative addition from a time when sophisticated analysis was not available. Structures that perform equally well can be obtained with few modifications to the design and functionality. Second, the failure load for the building appears to be linearly dependent on rise and thickness and not particularly sensitive. Even when pushed to the limits of the considered range of designs, the shell structure performed adequately under the considered load. This is a testament to the excellent structural properties of the hyperbolic paraboloid shell and the consequent widespread use. Lastly, modern analysis methods have a drastic effect on the efficiency of structural designs compared to methods used just 50 years ago.

The results presented in this chapter are pending journal publication.

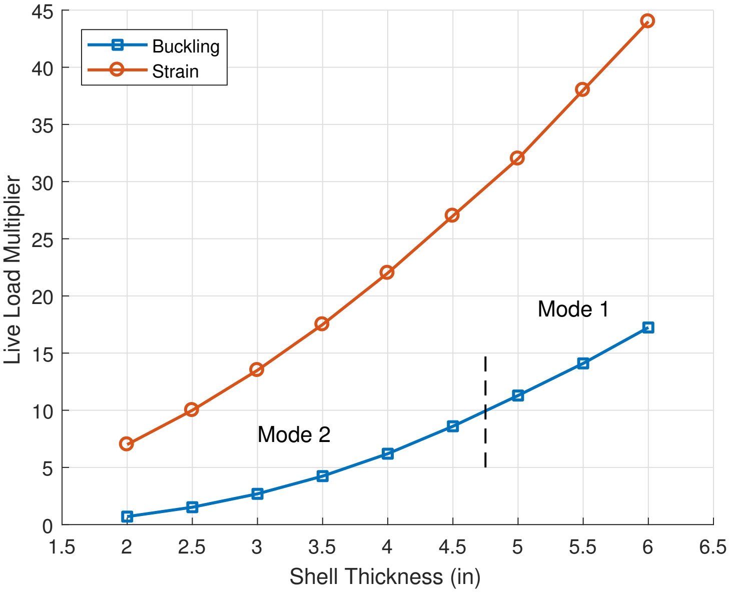

Figure B.8: Shell thickness design study results, with buckling modes labeled